Characterization of Mechanically Sheared Edges of Dual Phase Steels

Xin Wu and Hamed Bahmanpour

Department of Mechanical Engineering, Wayne State University, Detroit, MI 48202

Abstract

Advanced high strength steels (AHSS) received increased interest for light structures with improved performance, but it is sensitive to edge cracking during sheet metal forming. In this study mechanical sheared edges were characterized for three dual phase steels, DP600, DP780 and DP980, and for three die clearances and for edge orientation relative to the rolling direction. Microstructures and uniaxial tensile properties of the materials were studied first, and the sheared edges were examined by optical microscope and scanning electron microscopy. A new strain measurement was used for characterizing the deformation field of sheared edge, which shows the peak von Mises effective strain to be higher than 2 true strain. The strain quickly decreases from sheared edge to interior, leaving a shear-affected zone of 500μm or 31% of the thickness. The fracture processes and involved mechanisms were discussed.

(**Key words:** Advanced High Strength Steel, Metal Forming, Formability, Stamping, Mechanical Shearing, Edge Fracture, Simple Shear, Strain Measurement, Testing).

1. INTRODUCTION

In stamping operation of autobody manufacturing cutting processes are widely used, such as blanking, piercing and trimming. In production condition majority of these operations use mechanical shearing to break apart sheets along a designed cutting line at a high cutting rate or efficiency, while in tryout or for forming prototype parts laser cutting is often used, due to its advantages of high geometrical flexibility, reduced tooling cost and lead time. A large body of literature on piercing/blanking/trimming and flanging is available. An earlier review in metal piercing/hole-flanging was provided by Johnson [1], and some recent works for various materials

and dealing with some common issues in sheet metal cutting process and analysis can be found in [2-14].

It is well recognized that blank edge geometrical and microstructural features from cutting can give very important influence to the subsequent stamping operation, and it is more so for the sheet materials that have high strength and relatively low formability. For example, it is known that advanced high strength steels are sensitive to edge cracking, so that the features of sheared edges need to be better characterized, and their effect on stamping formability needs to be investigated.

In last decade significant effort has been made on development of advanced high strength steels (AHSS) and their applications [15], especially for lightweight automotive body structures. Application guidelines and special case studies were developed by steel industries worldwide [16, 17]. Among these advanced high strength steels, dual phase (DP) steel has its unique microstructural characteristics containing fine-grained martensite particles embedded within a ferrite matrix, produced through thermo-mechanical processing, resulting in combined ductility and strength at a low cost. This family of materials are globally uniform, but microscopically highly non-uniform in terms of its dual phase microstructure (with martensite particles at the scale of a few microns or less), and by varying the volume fraction of martensite phase, different strengths can be obtained at a better formability than that in regular high strength steels of similar strength. However, rather limited papers have addressed cutting of advanced high strength steels, in particular, the edge characteristics and its link to edge cracking of dual phase steels. The previous work of current interest include flanging of AHSS by [3], that indicates that if micro-cracks propagate mostly along the phase interfaces in DP steels the edge-stretch-formability is poor, while if cracking is through ferrite and martensite phases the formability is high. The difference in hardness is the dominant factor affecting the crack path and stretch-flange-formability. In addition, the volume fractions of phases also influence the formability. For single phase martensite steel a high edge strain gradient is in favor of high flanging formability.

In order to understand the mechanism responsible for edge cracking of AHSS, it is desirable to not only know the edge morphological characteristics and involved fracture mechanisms, but also to give a qualitative description of the pre-strain distribution at the sheared edge from a cutting operation. The strain distribution within the sheared sheet metal edge region has not been

reported, neither the method to measure the edge strain distribution. In terms of strain measurement method, surface grid measurement method has been well-developed and widely used in sheet metal forming industry environment for several decades, in which either circle grids or square grids were first placed on the sheet surface, and the measurements are made on the deformed grids in dimensions and orientations that can be correlated back to their initial ones, so that the local strain components or strain distribution can be obtained. The principle of using squared grids involving large strain analysis was given by Chu and Sowerby [??], and a simple explanation of this method is given by Marciniak, Duncan and Hu [18]. In comparison with the existing strain measurement method, the current problem of strain distribution measurement of sheared edge is significantly different and more challenging in three aspects: (1) The current problem needs to measure strains in the interior inside sheet metal thickness instead of outer surface, so that there are no traceable grids or nets that allows pre-preparation and correlation before and after shearing; (2) The length scale for the entire shearing affected zone is in the order of sheet thickness, which is much smaller than the existing surface strain measurement that deals with entire stamped panels or its local split/wrinkle regions at much larger scales; (3) the dominating strain components are shear strains that involve more angular measurement, while in previous surface strain measurement normal strain components are dominating and more interest.

In this paper, we report experimental observations on mechanically sheared edges of three dual phase steels, and investigated the effect of material (three DP steels), tool clearance (four levels) and shear orientation (rolling vs. transverse directions) on the characteristics of the sheared edges. We further developed a shear strain measurement method by tracing metal flow line tilting angle, and report the measured strain distribution on the sheared edges for the DP steels studied. Through this study a standard experimental procedure was developed for characterizing the mechanically sheared edges prior to stamping operation.

2. EXPERIMENTAL PROCEDURES

2.1. Materials and tensile tests

The as-received three advanced high strength dual phase steels, DP600, DP780 and DP980, provided by one of the US Auto Steel Partnership members, have a nominal thickness of 1.6mm

and produced from cold rolling. Uniaxial tensile tests were performed following ASTM E8-04 Standard for Tension Testing of Metallic Materials. Tensile specimens were machined to have 50.4 mm (2 inch) gauge length along 0˚, 45˚ and 90˚ to the rolling direction (RD), respectively, and with 12.7 mm (0.5 inch) gauge width. Tensile tests were performed at one of the laboratories of General Motors Corporation, in an MTS material testing system using a load cell of 90.9 kN (20,000 lb.) full scale and two extensometers, one in elongation direction and another in thickness direction, measured simultaneously. The measured load vs. extension data were converted to true stress vs. true strain curves, including non-uniform portion of the date that is known not part of the true stress-strain behavior of the material. Only the data within uniform deformation were used to fit powder-law strain hardening equation, and the powder-law exponent for each grade of DP steels and specified orientation was reported. In addition, based on plasticity incompressibility assumption the width strain of the specimen can be obtained from the two measured strain components, and the R-value of each test, which is the ratio of width strain to thickness strain, was reported as an average value within a specified uniform plastic strain range.

2.2. Mechanical Shearing

The shearing tests were based on a hole piercing operation performed at an industry stamping site. The tests used combinations of four piercing punches and two piercing dies, and produced round holes with four different die clearances at 5%t, 7.5%t, 10%t and 15%t where “t” is the blank thickness (1.6-mm nominal), to be used for further flanging operation to produce various flanging lengths (not included in this paper). The bland thickness, punches and die dimensions are listed in Table 1.

Table 1. Dimensions in piercing experiment

Cases	**1**	**2**	**3**	**4**
Blank thickness t (mm)	1.6	1.6	1.6	1.6
Piercing punch OD (mm)	15.8	15.72	10.84	10.68
Piercing die ID (mm)	15.96	15.96	11.16	11.16
Punch-die clearance relative to blank thickness (%t)	5%t	7.5%t	10%t	15%t

The punch-die clearances shown in the table are the design intent, while the actual tool clearances may slightly deviate from them due to tool elastic deformation, possible misalignment and other factors. Thus, whenever possible, the actual clearance was further verified from the optical micrographic image of the sectioned sample, from which the actual punch-die clearance can be measured as the spacing between the two vertical lines from the sheared outmost edge to the die supporting corner, which can be identified clearly if a burr was formed (which was not always the case). Later it was found that for most cases the deviations between the design intents and the actual measurements were insignificant for the reported results.

2.3. Microstructure and Fracture Examination

The sheared edges were examined under Optical Microscopy (OM) and Scanning Electron Microscopy (SEM) in following four consecutive steps, for all samples:

(1) OM Examination on replicas: The sheared surfaces were replicated using a 35 μm thick cellulose acetate film. (The preparation procedure is available from the vendor's website [1]), and replicas were made along the edges of round hole that were along rolling direction (RD) and transverse direction (TD) within about ±15˚, for obtaining more sheared samples without cutting/destroying the specimens. From replicas the burnish and fractured zone sizes were measured on digital images obtained from OM.

(2) SEM direct observation on the sheared surfaces: The sheared surfaces were examined directly from the sheared samples under SEM (Hitachi 2400, at 25 kV), for obtaining more detailed features at higher magnifications. The observations were made either from the normal direction to the sheared surfaces or, for burr morphology observation and burr height measurement, on the back side of the sheet pierced edge at a high angle between electron beam direction and the back surface normal (by tilting the sample stage 80˚ to allow revealing the projected burr height out of the back surface plane. The reported burr heights contained a system error of factor 0.985 (from sin90˚).

---

[1] Replica source: Jed Pellel Inc. P.O. Box 492477, Redding, CA 96049-2477. http://www.tedpella.com/replicat_html/44840.htm. Part No 44848

(3) OM observation on sectioned samples: Specimens were sectioned along the two hole central lines in RD and TD, cold-mounted using two-part epoxy [2], grinded and polished with the final pass at 0.03μm aluminum oxide particles. For revealing phase boundaries, samples were chemically etched with 0.5% HNO_3-methonal solution for about 10 seconds. OM examinations were performed on the sectioned surfaces, and digital images were taken, and if needed, measurements of dimensions and metal flow line tilting angles were made on the images with the use of a commercial image analyzing software.

(4) SEM observations on sectioned samples: For obtaining information on interior microstructures and micro-scale damages, the samples were further examined under SEM on the sectioned surfaces.

3. METHOD FOR LOCAL STRAIN MEASUREMENT

For the current plane-strain problem the local strain distribution within the sectioned plane was measured by tracing the interior metal flow line with references of martensite particle distribution. On etched cross-sections metal flow lines from cold-rolling and edge shearing can be clearly seen under OM (see Fig 1), due to existence of fine martensite particles that tend to align along the rolling direction before shearing. By tracing these flow lines, which were originally straight and parallel to the rolling plane (i.e. the sheet top/bottom surfaces) and then were bent/tilted within the shearing affected edge zone. By setting a coordinate system (x, y, z) for radial, hoop and thickness directions of the pierced edge, respectively, the flow line tilting angles, α, were measured over entire sheared edge zone of registered location (x, z), for more than 80 measurement points on each sample. The flow lines from straight to tilted can define the edge shear affected zone size, and the flow line tilting angle can be further converted to the strain components within x-z plane, as explained below.

[2] LECO Corporation, 3000 Lakeview Avenue • St. Joseph, MI 49085-2396 • Phone: 800-292-6141 • Fax: 269-982-8977, info@leco.com • www.leco.com

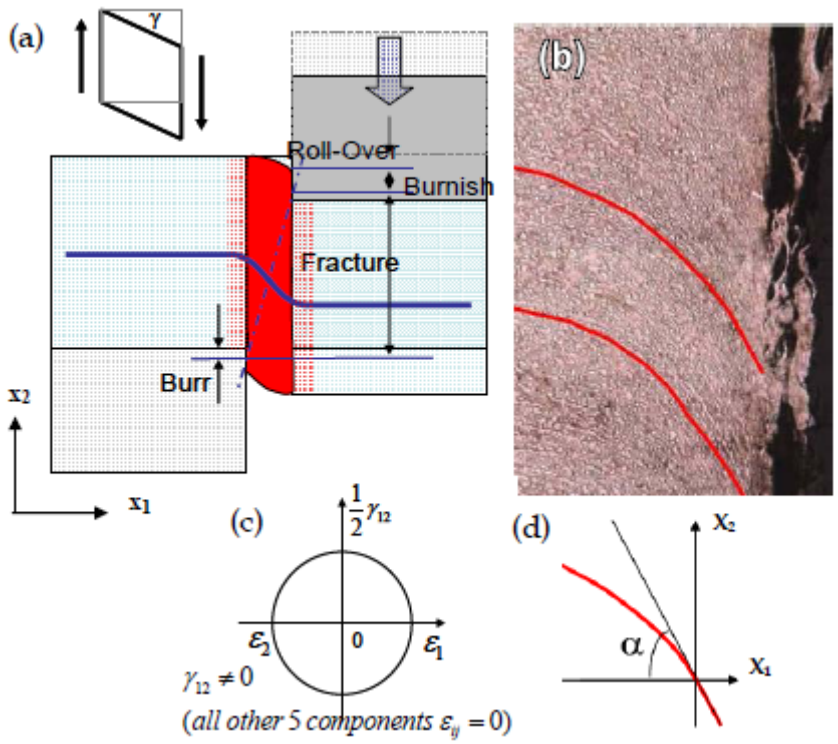

Fig. 1. Schematic of shear process with deformation mode of an element in simple shear (a) and its representation in Mohr cycle (c). The shear deformation resulted in tilting of metal flow lines that were originally horizontal from rolling and tilted to an angle α by shearing (b, d) that can be used for shear strain measurement.

Finite deformation formulation: Based on classical tensor analysis, the finite strain sensor components in (x, z) plane can be expressed as (see Appendix for more detail)

$$E_{ij} = \frac{1}{2}\left(\frac{\partial u_j}{\partial x_i} + \frac{\partial u_i}{\partial x_j} + \frac{\partial u_k}{\partial x_i}\frac{\partial u_k}{\partial x_j}\right), \textit{(i, j = x, z and } \kappa \textit{ is a dummy index over x, y, z)} \qquad (1)$$

The second-order derivatives, which are not considered in small deformation formulation, needs to be considered here. To obtain all three strain components within the x-z plane we need to know the displacement field of u and w, or the initial and final locations of each given material particle, which are not available. However, without actually mark the material particle we may be able to trace the particle initial and final location if we introduce a simplification assumption that $u \approx 0$, which may be acceptable under the current firmly clamped condition and with very narrow punch-die clearance gap. This assumption not only leads to all derivatives of u to be zero,

but also leads to $\frac{\partial w}{\partial z} \approx 0$, because from volume conservation of plasticity (ignoring the micro-cracking), any area element needs to remain constant area, so that if no displacement u there will be no scale changes in x direction, nor in z direction. Thus, all the flow lines must remain parallel. This may also be acceptable from experimental observations that for all sectioned samples there is no noticeable change of flow line spacing and total thickness, or if any, the change of w is much less significant along z direction than that along x direction. With this assumption we can know for each material particle the x-coordinate after shearing is also the x-coordinate before shearing, and the z-coordinate after shearing can be tracked back to its original z-coordinate from its corresponding flow line when it was still straight, and the actually marking and registration of material before shearing is not needed.

Now let's use *k* to be the slope of the flow line in deformed sample coordinate, $\frac{\partial w}{\partial x} = \tan(\alpha) = k$, and from Eq (1) the only two non-zero tensor strain components are:

$$E_{xx} = \frac{1}{2}\left(\frac{\partial w}{\partial x}\right)^2 = 0.5\,\kappa^2 \tag{2}$$

$$E_{xz} = \frac{1}{2}\left\{\frac{\partial w}{\partial x}\right\} = 0.5\,\kappa \tag{3}$$

All other components are zero. And von Mises effective strain is given by

$$E_{eff} = \sqrt{\frac{2}{9}\left[\left(E_{xx} - E_{yy}\right)^2 + \left(E_{yy} - E_{zz}\right)^2 + \left(E_{zz} - E_{xx}\right)^2 + 6\left(E_{xy}{}^2 + E_{yz}{}^2 + E_{zx}{}^2\right)\right]}$$

$$= \frac{2}{3}\sqrt{E_{xx}{}^2 + 3E_{xz}{}^2} \tag{4}$$

Or,

$$\boxed{E_{eff} = \frac{k}{3}\sqrt{3 + k^2}} \tag{5}$$

At a small flow line tilting angle ($\alpha << 1$ radian) Eq (2) reduces to zero, and Eq (5) reduces to $E_{eff} = k/\sqrt{3}$ (that is the solution of small deformation formulation). But at a large k or tilting angle (α approaches $\pi/2$) the normal stress term E_{xx} becomes dominant, and $E_{eff} \approx k^2/3$. This

can be seen more clearly in Fig 2. At 45˚ the normal stain and shear strain have the same value of 0.5 and the effective strain is 2/3.

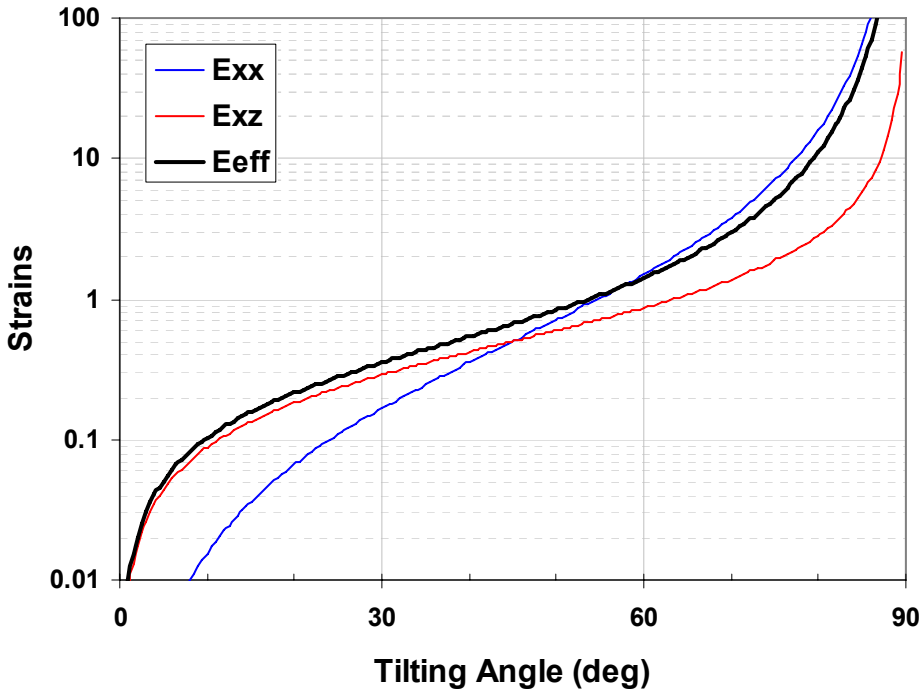

Fig. 2. Strain components and effective strain as a function of flow line tilting angle. All other components are zero.

4. RESULTS

4.1. Microstructures of as-received materials

Typical microstructures of as-received three DP steels are shown in Fig 3 in rolling, transverse and thickness directions (respectively labeled as RD, TD and t), obtained from OM. To estimate martensite volume fractions, the digital images were further processed with an image analyzing software, and the results are shown in Figure 4. The large variables in three orientations are due to limitations in image analysis system, sampling size used, and the capability of the image analyzing software. The micrographs shown here can not full description the materials' microstructures, but can only provide a semi-quantitative measure that is needed for better understanding the edge features reported in the rest of this paper. For these and many additional samples examined, several notable microstructural features are worth mentioning:

- Martensite phases are shown as isolated particles, and they tend to align preferably along in rolling direction.
- The average area fractions of the martensite phase in DP600, DP780 and DP980 are 13.7%, 22.9% and 47.3%, respectively.
- At a high martensite volume fraction (e.g. for DP980) martensite particles have a high chance to connect with each other, forming 3D network.

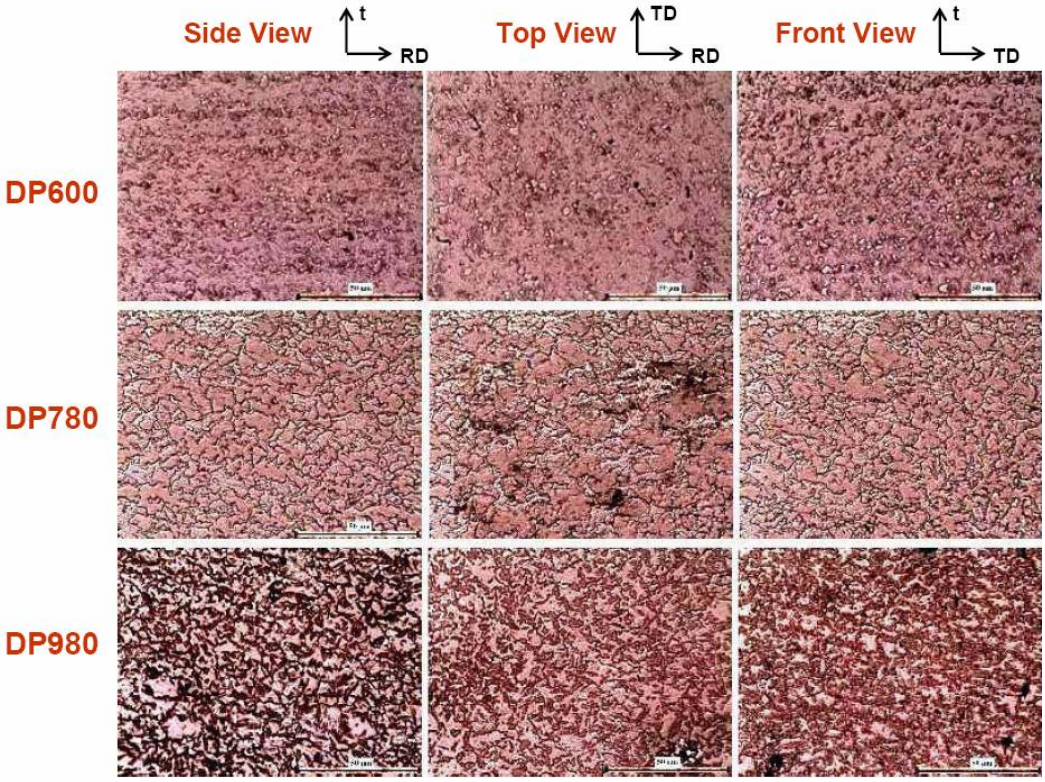

Fig. 3. Optical micrographs of three DP steels on three sectioned planes, and the micrographs from an image processing software that provided statistical information on individual martensitic particle area and other geometrical features, from which the average volume fracture over three sections were reported in the table. The scale bar is for ?? μm.

4.2. Tensile properties

The tensile true stress vs. true strain curves of the three DP steels are shown in Fig 4. By regression of true stress-true strain data using a power-law, two strain hardening exponents were obtained from two uniform strain ranges, i.e. n_1 value calculated from the elongation ranging

from 4% to 6%, and n_2 value calculated from the elongation ranging from 5% to 10% or at the end of uniform strain if it was less than 10%. The $\overline{R}$-value, ($\overline{R} = \varepsilon_w/\varepsilon_t$ where w and t denote width and thickness directions) was calculated as an average value from 0.2% yielding point to the end of uniform elongation. All the results are listed in Table 1. As can be seen that from DP600 to DP780 and DP980, the yield strength and ultimate strength increase, and the total elongation and the strain hardening rate (n-value) decrease, which is in consistent with the increase in martensite volume. In addition, the total elongation is higher in RD than that in TD.

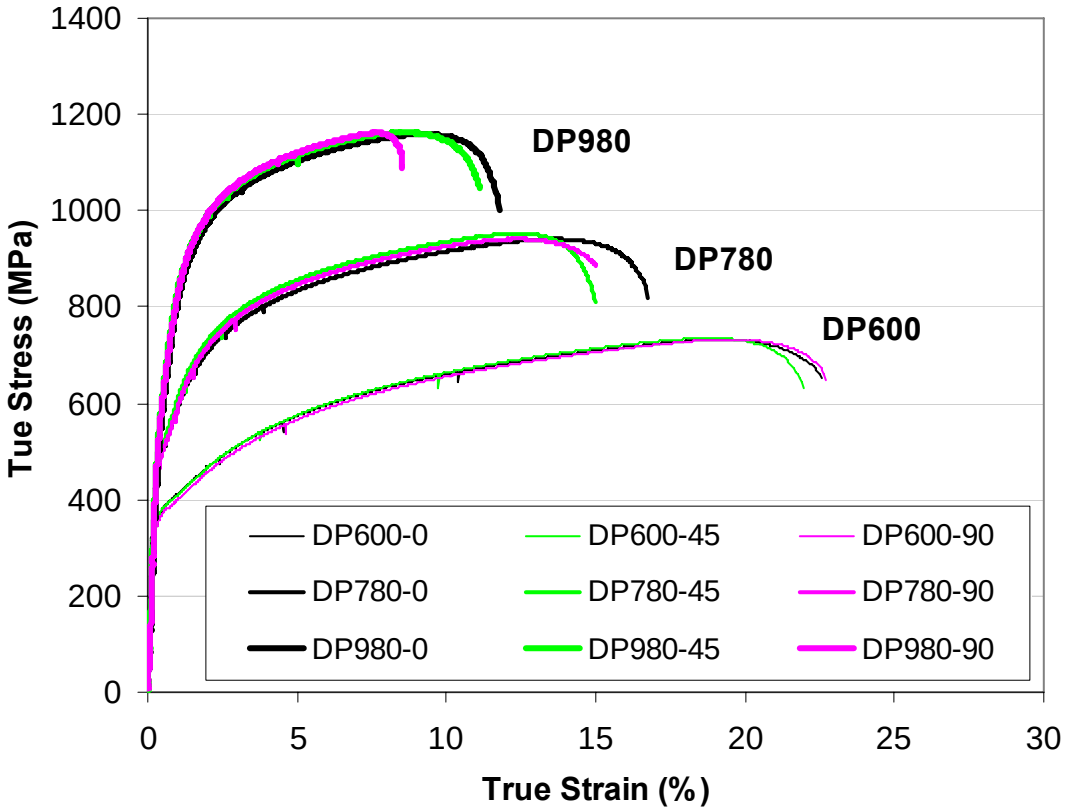

Fig. 4. True stress vs. true strain curves of the as-received three DP steels from uniaxial tensile tests. Each material was tested along 0˚, 45˚ and 90˚ to the rolling direction as specified by the ending digits of material labels. The data after necking are also included in the curve, but were not used for the fitting of power-law strain hardening equations.

Table 2. Summary Results from Tensile Test

Sample ID	Peak Stress (MPa)	0.2% Offset Yield Stress	% Uniform Elongation	%Total Elongation	n_1 Value	n_2 Value	$\overline{R}$ -

		(MPa)					Value
DP980-0	1064	608	7.7	12.5	0.10	0.09	1.10
DP980-90	1078	628	7.5	8.9	0.10	0.09	0.73
DP980-45	1073	637	7.4	11.7	0.10	0.09	0.93
DP780-0	830	496	11.9	18.2	0.15	0.12	1.07
DP780-90	838	496	10.8	16.2	0.15	0.11	1.07
DP780-45	847	502	11.4	16.2	0.15	0.11	0.80
DP600-0	611	367	16.5	25.3	0.22	0.18	1.04
DP600-90	609	358	18.0	25.5	0.22	0.18	0.84
DP600-45	615	371	17.1	24.5	0.22	0.18	0.87

4.3. Morphology of Sheared Edges

(1) Distinction of four edge zones:

A typical sheared edge is shown in Fig 5, viewed from sectioned surface. From the figure the four characteristic edge zones can be clearly distinguished, as marked in Fig 5(a). The local enlargement in the burr zone is shown in Fig 5(b), from which the die contact edge (corner) can be identified, so the actual die clearance between the punch-sheared edge and the die edge was measured from the micrograph, which is very close to the specified 5%t for this sample. From the observed shear edge morphology, the characteristics of each edge zone and the formation mechanisms are briefly described below:

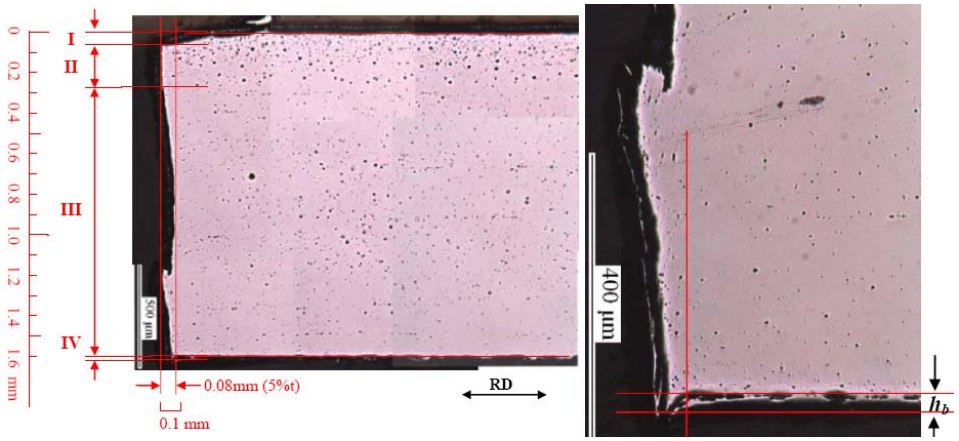

(a) (b)

Fig. 5. A sectioned DP780 sample that shows geometrical features of mechanically pierced edge, consisting of four edge zones: I-Roll-over, II- Burnish; III-Fracture; IV-burr, see (a). The local enlargement of the burr geometry is shown in (b).

a) Roll-over zone: With the punch pressing and die supporting, the metals under punch contact was moving downward in compression and the surface outside the punch contact was under elastic and plastic bending, up to a stage when the punch edge cut through the sheet surface, resulting in a curved surface outside the punch contact. The depth (or roll-over zone height), radius and the profile of the curved surface were directly affected by the ability of the sheet metal to hold the surface flatness before being intruded by the punch, so it is largely determined by the material property (mainly strength and hardness) and processing parameters such as punch-die clearance, cutting edge roundness (from initial machined state to wear out) and sheet thickness.

b) Burnish zone: With punch further advancing, punch penetrated into the blank interior, leaving a set of straight and vertical scratches on the sheared sheet edge. At certain depth a main crack initiated at a location with highest tensile stress, which should be in the neighborhood of tool cutting edge (apply for both punch and die). This main crack location defined the ending point of burnish zone. Thus, the size of this zone is controlled by the crack initiation under the applied shear stress, which can be closely related to the Mode-II fracture strength of the material.

c) Fracture zone: With punch further advancing, the initiated crack continued its way to propagate though the rest of the thickness section, either by stable growth (initially), or might become unstable when it reached a critical crack length before reaching the end of the thickness. Both stable and unstable crack propagation would produce rough fractured surfaces for this DP material family.

d) Burr zone: As shown in Fig 3(b), at the final stage of the fracture development and under the effect of compressive stress state from bottom die support, small amount of metal outside the die corner remained in connection with the slug, causing a delay in fracture, and finally separated by tension and tearing, leaving a set of irregular ligaments extending out of the sheet thickness range.

(2) Random nature of fracture path

Figure 6 shows several shear-fractured edges in sectioned views. It can be seen that fracture path may not necessarily go through the line linking the two tool edge corners: In one extreme case (Fig 6a) the sheared edge went along vertical direction through the thickness, and the entire fracture zone disappeared and replaced by the burnish zone. In another extreme case (Fig 6c), the fracture path ran away from the punch vertical moving direction and got into the die supporting region, and finally hit the die top surface, leaving no burr formation. In this case the separated metals in the left side of the separation would be larger than the clearance zone and would interference with two rigid tools, so it is believed that the metals outside the tool gas zone must be sheared and smashed into separate pieces, and when the punch retracted back the open space became available for the separated pieces outside the gap zone to fall out. Many cases were between the two extremes, with the shear and facture occurred within the tool gap zone, see Fig 6b. Comparisons between RD and TD of the same samples are provided in Fig 6(a, c) for DP780 at 5%t and Fig 6(d, e) for DP980 at 10%t, both showing very different edge profiles between RD and TD. If we define a crack path angle β as the angle from vertical line of the punch edge, a general trend is that the fracture path tends to go along smaller angle for the cutting direction perpendicular to RD (the sectioned image marked RD) than for the cutting along TD, and a material with a higher strength (DP980) and smaller tool clearance (10%) tends to have a higher path direction angle the that with a lower strength (DP780) and a smaller tool clearance (5%). In all, for the dual phase steels the crack path angle β can be in a wide range, and the main crack might develop from the tool cutting edges from top (punch) or from bottom (die), as shown schematically in Fig 6(f). In addition, within the shearing zone and its neighborhood multiple subcracks and microcracks could develop, and the main crack was developed to a variety of edge profiles in complex shape rather than a straight one, probably related to the variety of ways to link many microcracks. For example, the edge path profile shown in Fig 3 seems the result of a main crack from top with a high path angle β and a crack from bottom, and the two linked when the top crack propagated to cross majority of the thickness. Other edge profiles shown in Fig 6 do not have such a deflected edge profile, but with different path angles. This highly random fracture nature of dual phase steels was not seen in regular high strength steels and other ductile metals (e.g. aluminum and copper alloys), or at least not at this degree of randomness and

variety, and it may be associate with the highly inhomogeneous microstructures containing two phases of significantly different properties.

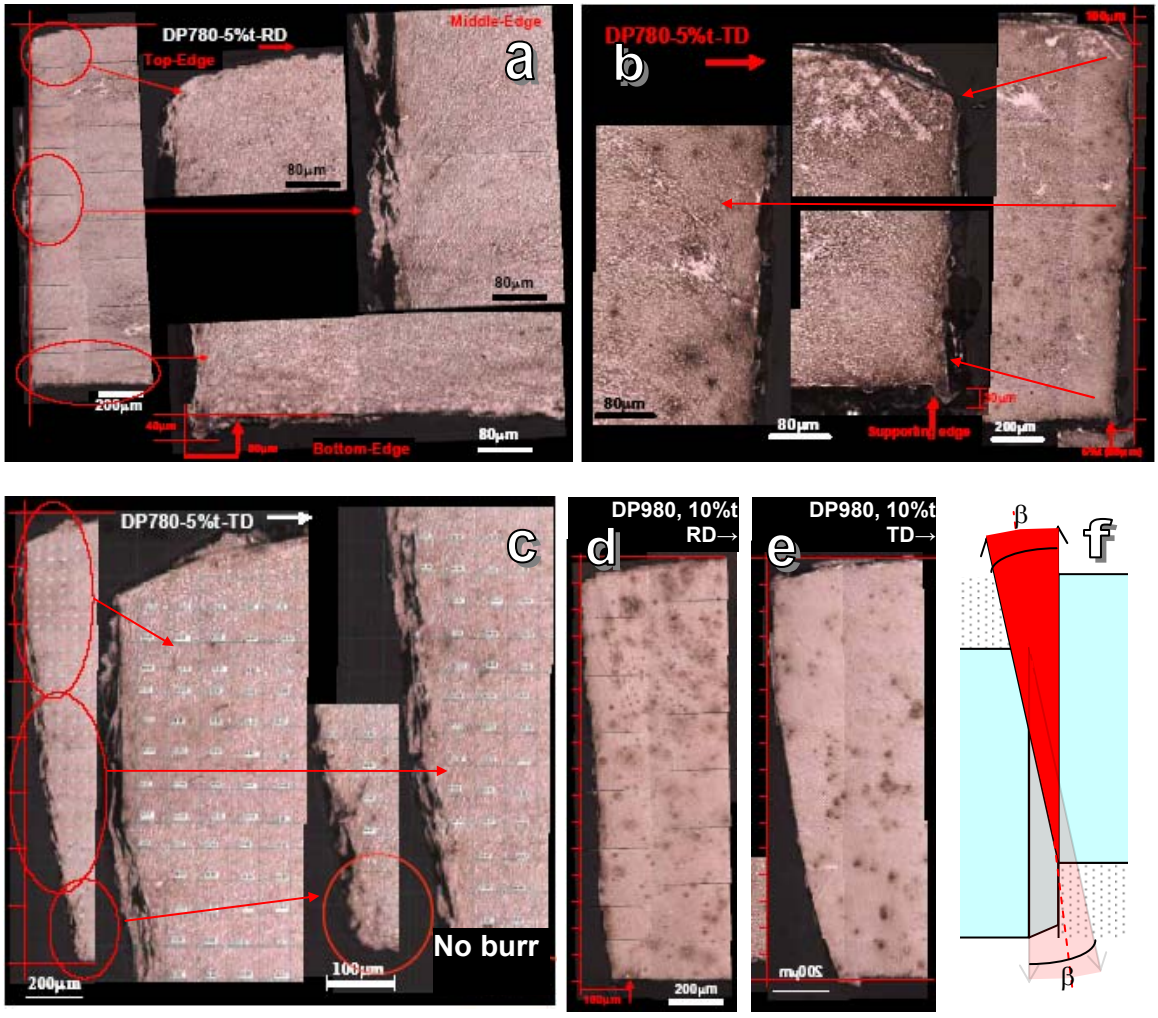

Fig. 6. Randomness of fracture path in shearing DP steels, resulting in incomplete formation of four-zone edge, such as full burnish zone (a), or missing of burr zone (c), and between the two (b). The edges in RD and TD of the same sample are comparable from the pairs of (a, b) and (d, e). The upward arrows at the bottom of the samples are the die supporting edge locations. A schematic in (f) shows the crack path range in certain angle β that may develop from both top and bottom sides.

(3) Observations of As-Sheared Surfaces

a. Burnish zone characterization

Figure 7a shows a normal view of the as-sheared surfaces for the DP780 sample at 5%t clearance, with the burnish zone almost covered entire thickness (if ignoring the minor roll-over zone and burr zone). A close look of this sheared surface reveals three detailed features:

- There exists a continuous horizontal groove line at the depth of about ¼ thickness from the sheet top surface, similar to the position of a regular burnish zone ending point, see Fig 7(A).
- While entire thickness was sheared by the punch as clearly seen from the scratching markers, there exist many small patches that were also scratched by the punch, but not on the same sheared plane, but below it, see Figs 7(B, C) for two local enlargements. The dimensions of these patches are at much larger length scale than the martensite particle size.
- These "low-land" patch zones have a flat bottom and with punch scratching markers on it in the similar pattern to that outside the patches and they are in various sizes and shapes. Further observation indicates that the population of those patches is relatively less above the horizontal groove line, and more below it and increases the population from top to bottom. In addition, on upper portion of the thickness most patches have a "Λ" shape or the top half of a circle with the opening facing down, while toward the bottom many of them show as a full circle or closed loop, within which the tool scratching marks can be seen even more clearly.

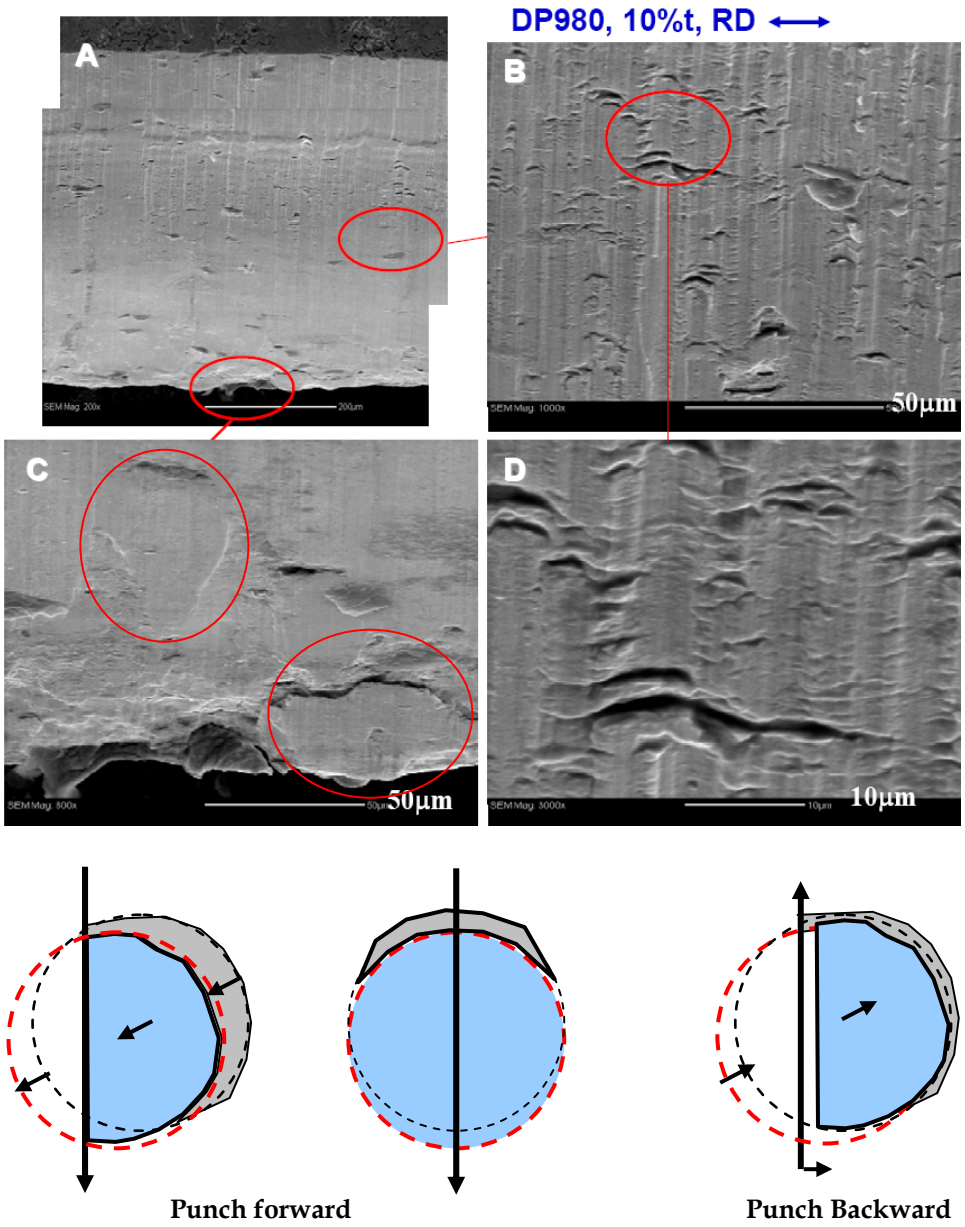

Fig. 7. Top: Morphology of sheared surface and its local enlargements of a DP780 sample at 5%t clearance. The punch scratching marks covered entire sheared surface, on which many scratched patches are not co-planar but below the sheared surface. Bottom: Demonstration of the formations of "Λ"-shaped cracks and sink surface patches, due to interaction between cutting shear plane and martensite cluster (shown in circle)

How can the tool scratching marks be not co-planar on the same sheared surface but on different planes is not so easy to explain, and one explanation is discussed here. Since it is not possible for the rigid punch (or die, whichever produced the sheared surfaces) to reach different surfaces and produce sheared/scratched surfaces at different planes during its cutting cycle when moving in vertical direction, it is only possible that those patches were formed after they were scratched, after which they were moved away from the shearing plane. More over, one necessary condition for this to happen is that there existed certain spaces behind the shearing surface to allow part of the scratched regions to move inside away from the shearing surface. Based on these reasoning the "low-land" patch formation process is described as follows (as demonstrated in Fig 7): Within the punch forward cycle and when the punch moved to about ¼ of the thickness a burnish zone formed as usual, producing a horizontal crack opening line. But the crack was not fully developed to cause unstable propagation and to reach the bottom of the thickness, due to very narrow punch-die clearance (5%t) that confined the separation of material. This resulted in the further or secondary shearing in the remaining metals within the gap zone during punch continued advancement, along with formations of many microcracks behind the sheared surface. These microcrackes tended to develop along the weak link, which appeared to be the boundaries of martensite clusters at a relatively larger length scale than the martensite particle size. Also the cracking along the martensite cluster boundary took a progressive process starting from separation at the top boundaries, then extended to the back side of the cluster, and finally extended to its bottom to form a complete loop (but still have many local connections with the base metal). Associated with the cluster boundary separation was the clearance generation on top and back of the cluster, leaving certain spaces on their back, see Fig 7(a). By accumulation of the microcracking the more the punch displacement, the more severe the micro damage development was. At the end of punch forwarding the sheared metal should still remain in full contact with the punch side wall or within the same sheared plane, but certain spaces were generated behind those damaged martensite cluster boundaries. Upon punch reversal motion those partially separated martensite clusters were pushed back to the base metal under the punch frictional force, but blocked by the cavity walls. As a result these patches separated from the punch side wall and moved back to fill out these upper and back clearances, forming observed low-land patches, see Fig 7(b) for clusters that only developed on top portion of martensite clusters at early stage, which appeared more often in upper part of the thickness, and see Fig 7(c) for those well

developed damages along martensite clusters boundaries with open space on back side, which appeared more often in the lower part of the thickness. Therefore, the shape and size of these sinking surface patches can reflect, at certain degree, the size, shape and severity of microcrackes behind the sheared surface, and the total volume generated from these sinking patches moving away from the shearing surface provides a low-bound estimation of the total volume of cavities. The extra volume was gained by metal flow to unconstrained area during punch forwarding motion, for example to cause bending of slug and thickening of deformation zone.

b. Burnish Zone Height

The burnish zone and fracture zone occupy majority of the sheared thickness, so that a short burnish zone means an earlier occurrence of fracture and a larger portion of fracture zone. Here we provide more examples of the as-fractured edge surfaces to show the morphologies of as-fractured surfaces with complete four-zone feature, see Fig 8.

Comparing die clearance at 10%t in Fig 8(a, c) and 15%t in Fig 8(c,d), smaller die clearance tends to produce a smaller fracture zone, due to the die constraint that delays fracture. Comparing DP600 in Fig 8(a,b) to DP780 in Fig 8(c,d), a softer/more ductile material tends to delay shear fracture.

Further examination of fractured surfaces shown in Fig 8 reveals some interesting surface topological features. It was found that the sinking surface “low-land” patches also existed on fracture zone, as shown in circled areas. Tool sheared scratches were found in Fig 8(d) within a large patch, while outside patch are fractured rough surface. In this case the fracture occurred after the sheared scratches were formed and pushed inside, in addition, during this pushing movement the cluster (the volume of the patch) and the surrounding base metal had a severe shear, leaving a smooth sheared surface in the depth direction on the wall between the patch surface and the fractured surface. In comparison with Fig 5 for a complete burnish zone case, here the secondary burnish zone fully explored to show both fractured surface and the sinking patches as a way of grouped metal movement, once again indicating a non-uniform microstructure effect on the fracture. Also shown in Fig 8(e,f) is an incomplete development of surface crack with a “Λ”-shaped crack and its local enlargement.

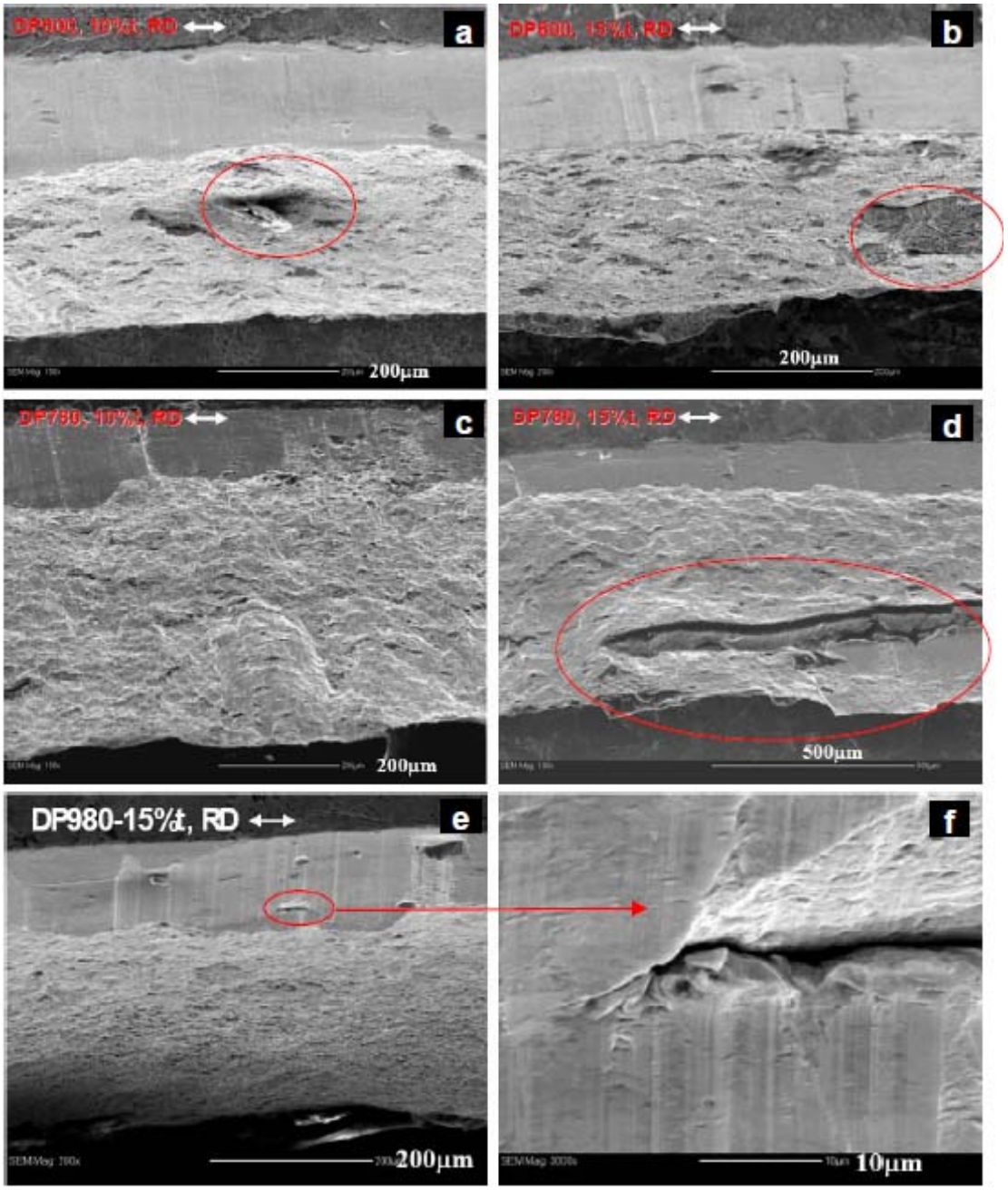

Fig. 8. Some examples of sheared edge surfaces: 10%t clearance (a, b) tends to give larger burnish zone than 15%t (c, d); and within burnish zone there are many cracks not fully developed to the final main crack (e and its local enlargement in f).

In order to quantify the trend of burnish height as a function of material, orientation, and die clearance, we need to obtain statistical features from a large sampling size. With limited shear samples (repeat runs), the replica technique was used to get more measurements from single sample. Fig 9 shows summarized replica images.

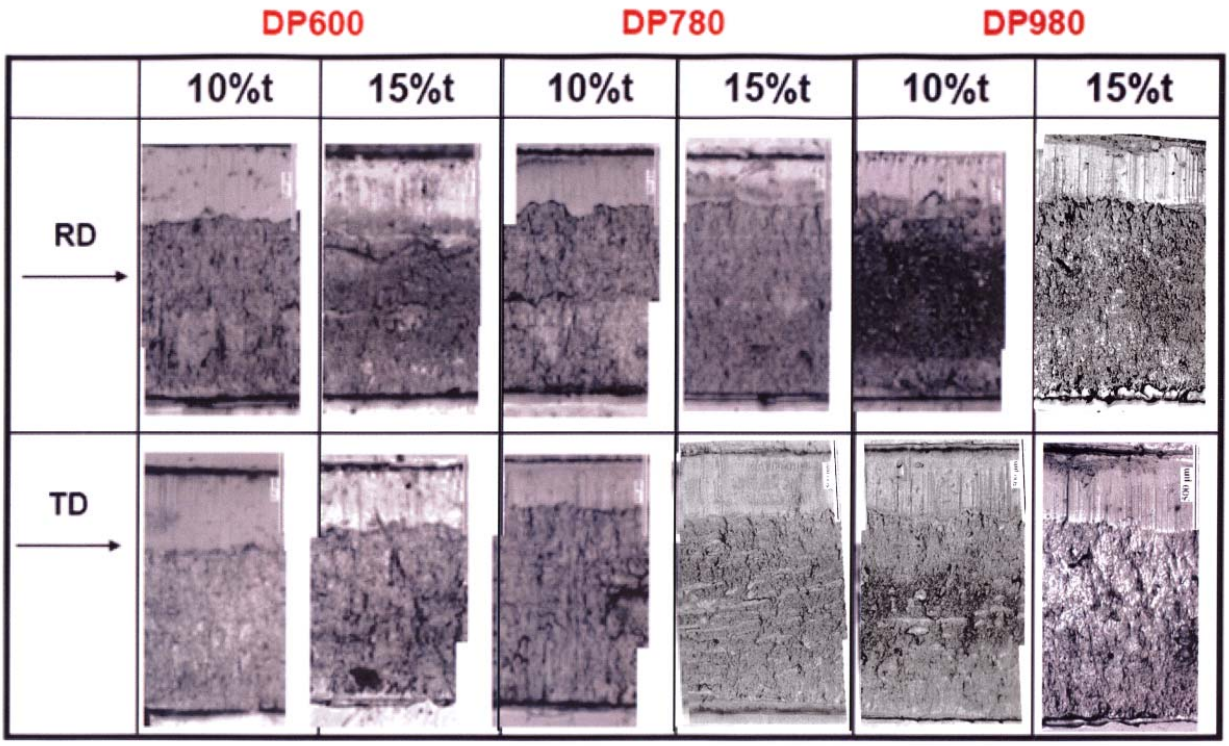

Fig. 9. As-fractured surfaces observed from Replica technique, showing burnish and fractured zones for different materials and blank orientations, and die clearances.

Figure 10 shows the measured mean values for burnish zone heights and standard deviation along with the scattering data bands, for all different conditions specified. The trends on burnish height are as follows:

- The effect of material type on burnish height: DP980 < DP 780 < DP600;
- The effect of shear direction relative to rolling direction: shear along RD < shear along TD;
- The effect of die relative clearance on the burnish height: take average of RD and TD, we get a relative weak trend: for burnish height 15%t < 10%t.

As a general trend, burnish height decreases with decreasing material ductility, reduced fracture strength, and increased material constraint within the deformation zone (die clearance here).

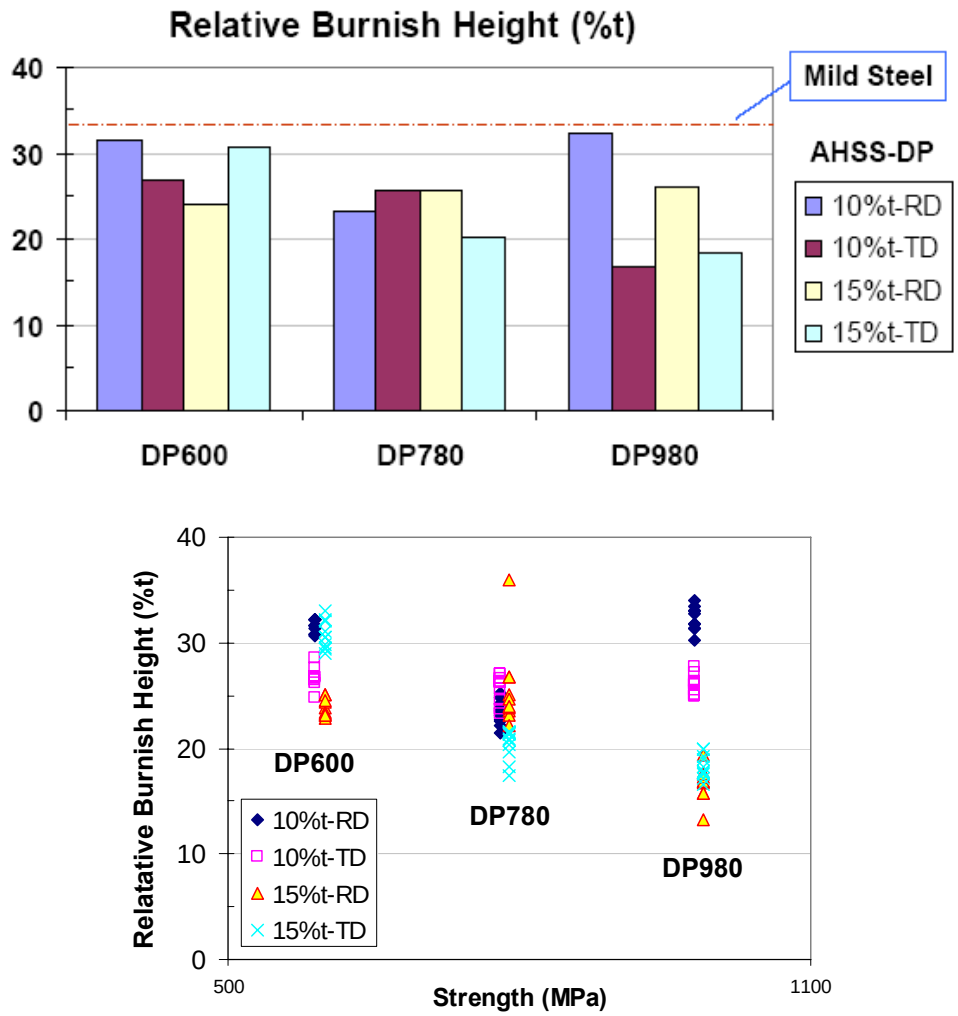

Fig. 10. Relative burnish heights of various materials, die clearances and along two sheet orientations in RD and TD (top), and scattering of the measured data (bottom).

c. Burr Height and Burr Formation

The morphology of burrs can be observed under SEM when the sample was viewed from the back surface that was in contact with die supporting surface, and when the sample surface normal direction is tilted to 80˚ from the electron beam direction, see Fig 11. It can be found that along the edge line (hoop direction of the pierced hole) the burr height varies widely, including many burr-free areas. This is largely due to the crack path changes along the hole hoop direction, as seen from the fractured surface in Fig 9(c,d). This is again in supporting the random nature of fracture of these high-strength materials.

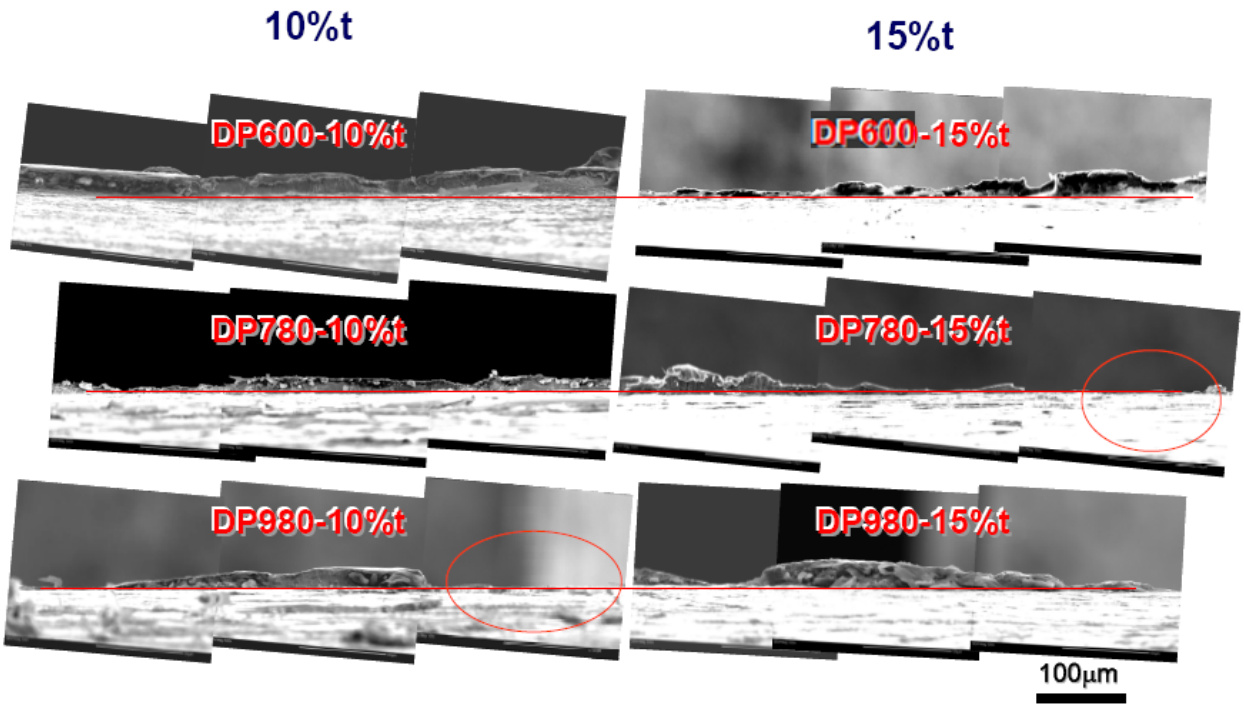

Fig. 11. Burrs observed by SEM with e-beam direction in 10 to the back surface of the pierced samples, for various materials and die clearances indicated.

Burr heights along the sheared edge were measured from original high-resolution SEM images over more than 50 points, for each sample, and the results of the mean burr height and standard deviation are shown in Fig 10. The summarized trends are given in Table 4. The effect of die clearance to the burr height is not very obvious, and will be discussed later.

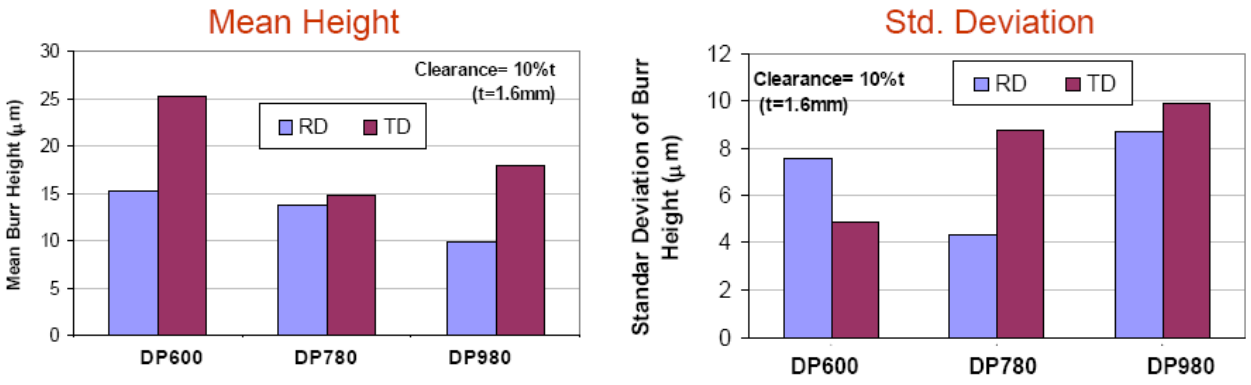

Fig. 12. Measure mean heights and standard deviation of three DP steels sheared along RD and TD (clearance at 10%t)

Table 3. Summary of the Trend in Burr Height

Effect Burr height	Material Grade	Cutting line Orientation
Mean:	DP600 > DP780 > DP980 (Except for DP980_TD)	RD < TD
Deviation:	DP600 < DP780 < DP980	(Not clear)

(4) Summary of edge zone geometry

For all the combinations of shearing parameters, we have die clearance relative to the sheet thickness (5%t, 10%t, 15%t), grade of DP steels (DP600, DP780 and DP980), and the shear line direction (0 for RD and 90 for TD), and the output responses are the heights of the four sheared edge zones. The results are plotted in Fig 13. In this Fig, in order to reveal the effect of each input parameter, a linear rescaling of inputs was performed so that the range of input variables is linearly transformed to the range of (-1, 1) using the formulae:

$$x' = x'_0 + \frac{x'_2 - x'_1}{x_2 - x_1}(x - x_1) = -1 + \frac{2}{x_2 - x_1}(x - x_1) \quad (1)$$

Where x and x' are the input variables before and after the linear transformation, and the subscripts 1 and 2 denote the lower and upper bounds, which are -1 and 1 for x'. The output effects (zone heights) are fitted by linear or quadric polynomial regression, for 2-level and 3-level variables, respectively. The scattering of the data are mainly from the effect of other input variables. Note that this set of experiments does not strictly follow (but very close) an orthogonal matrix as that in a standard Design of Experiment (DOE) setting arrangement, in which each variable has equal probability to appear in the variable combinations. (Based on DOE with half-orthogonal arrays we only need (2x3x3)/2=9 settings or experiments without repeats). But in the current study it was intended to provide a full factorial study for generating new understanding of shear physical processes, but here we missed 3 settings (two set of 5%t tests and one output measurement).

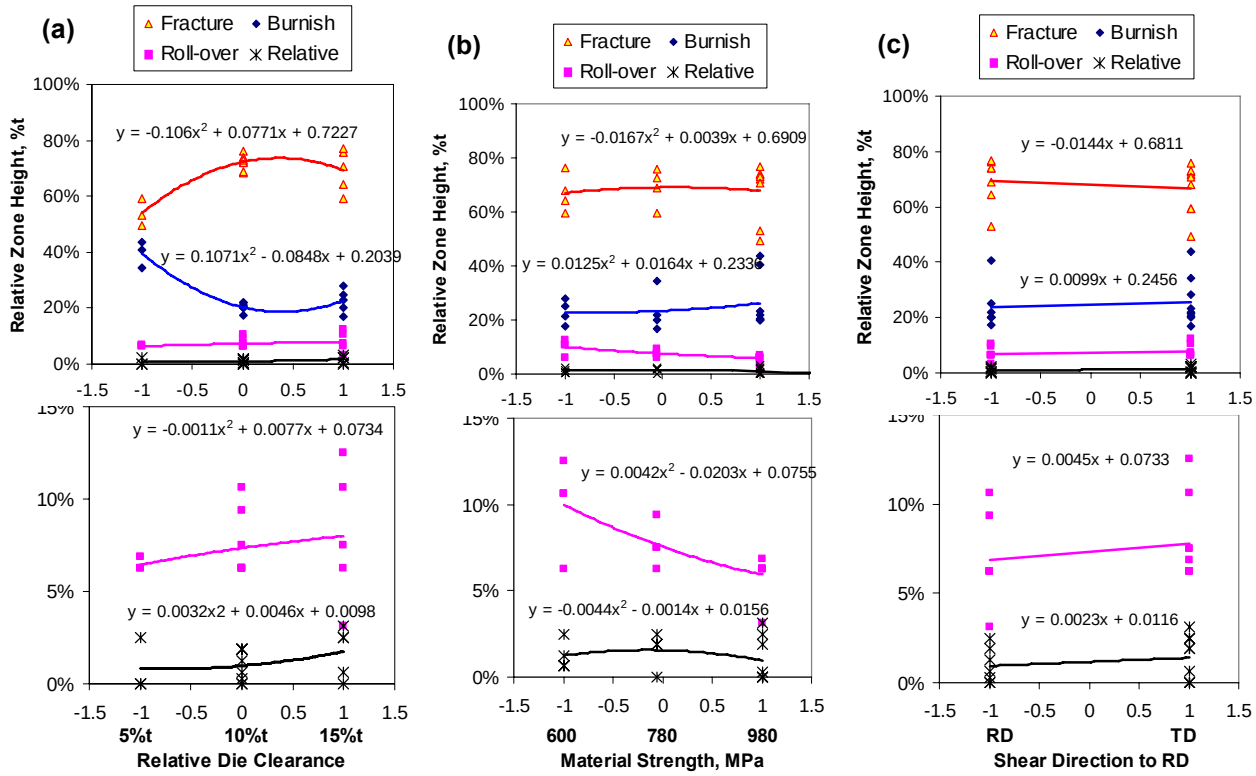

Fig. 13. Edge Zone Heights as a function of processing parameters: (a) relative die clearance, (b) material strength (or grade), (c) shear direction, or the shear line angle to the rolling direction from 0˚ to 90˚. The bottom plots are the local enlargements of corresponding top plots.

From Fig 13 the three processing variables have the following effects on the edge zone heights:

(1) Die clearance: with increasing in die clearance both burr and roll-over increase, while the burnish zone height decreases initially and then increase later. In small clearance region (5-10%t), due to the tool constraint that postpone metal fracture within a narrower tool clearance. In larger clearance region (10-15%t) the burnish zone height increases with increasing clearance, due to reduced intensity of local shear stress, which is less concentrated for equivalent punch displacement.

(2) Material strength: increase in material strength results in reduced burr height (not so obvious for DP600), significant decrease of roll-over zone height, and slight increase in burnish zone height.

(3) Shear direction relative to RD: increase in shear line angle to RD from 0 (RD) to 90 (TD) results in the increase in burr and roll-over heights. It also slightly increases in burnish zone height.

4.4. Edge strain distribution

The full quantity of engineering shear strain is simply the slope of the metal flow lines that were originally parallel to the sheet surface due to rolling, and after shearing tilted to an angle α, as shown in Fig 14 or the tangential of the line tilting angle, see Fig 15.

(2) Shear-Affected Zone Size and Measured Strain Distribution

By tracing the metal flow lines and measure the tilting angle distribution over the sheared zone (as shown in Fig 14), the shear angle and strain for each specified location were obtained, within the (x1-x2) coordinate system where x1 was from outmost sheared edge to interior, and x2 was from top sheet surface to bottom of the thickness. The edge shear angle and effective strain distribution for all three DP steels, two die clearances and two shearing orientations are shown in 2D plots, in which the arrows show and flow line tilting angles, and the arrow lengths are the magnitudes of equivalent von Mises strains.

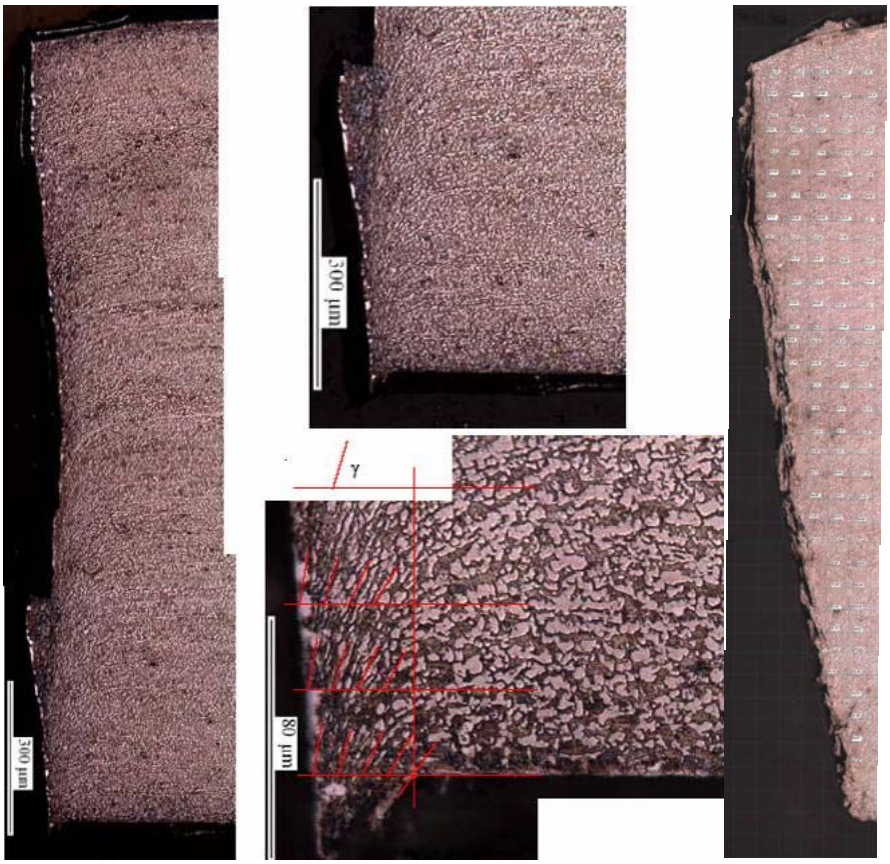

Fig. 14. Examples of strain distribution measurement from the tilting angles at given locations. The flow-line angle to the rolling direction allows obtaining the engineering shear strain

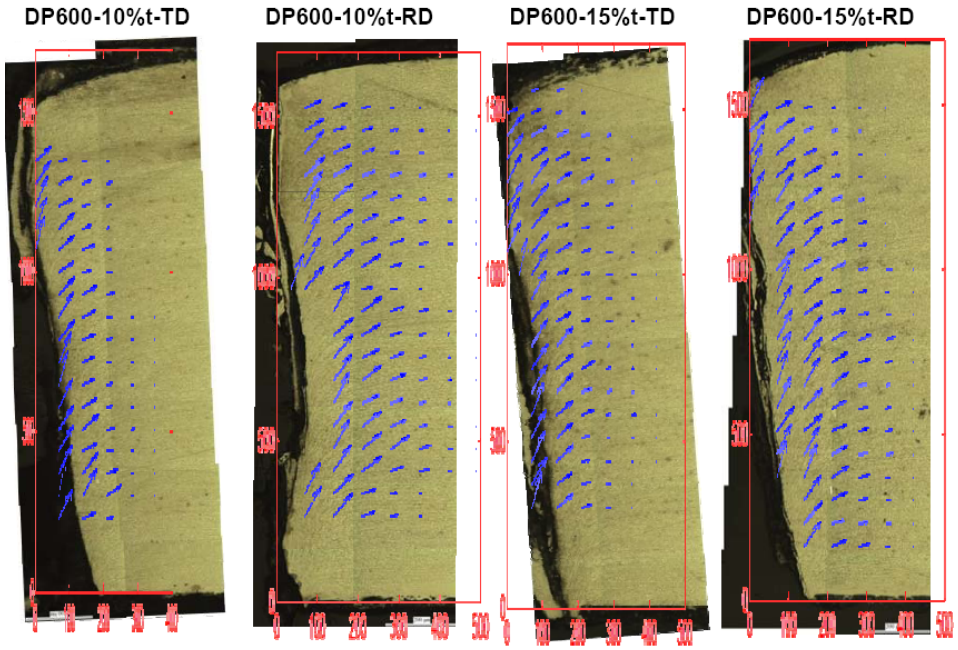

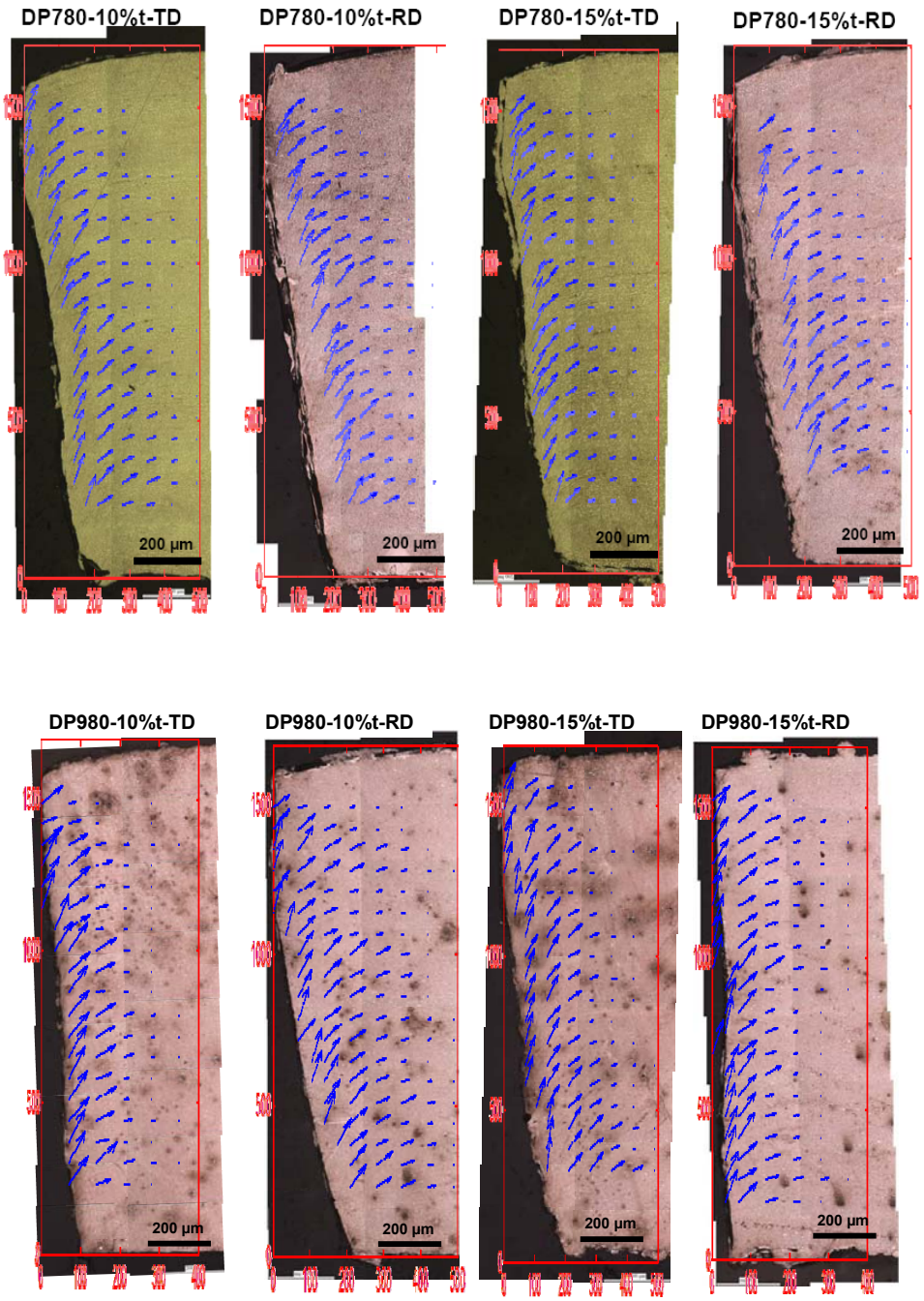

Fig. 15. DP600 cross-sectional views of sheared edges at different piercing die clearances and sectioned planes (rolling or transverse directions), with measured metal flow field.

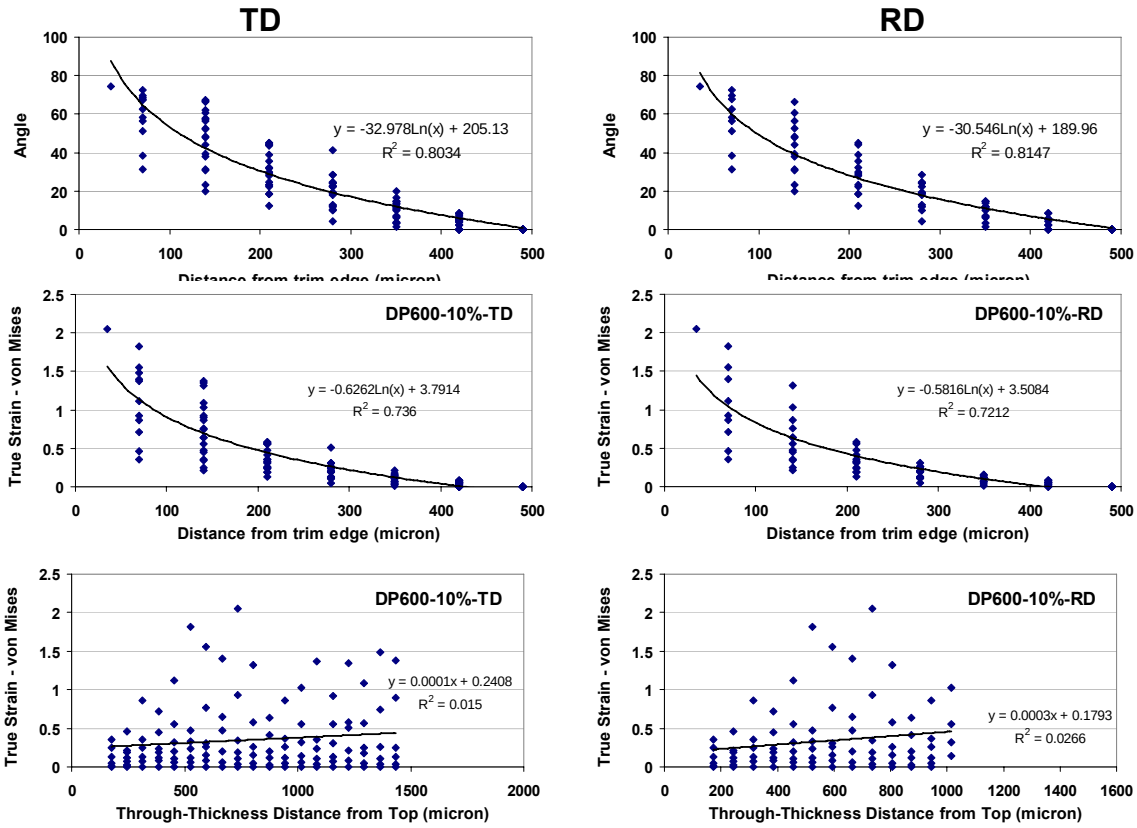

Fig. 16. DP600, 10%t. Measured angles and true equivalent strain distribution from edge to interior, and from top to bottom of the thickness, with the shear lines in RD and TD, respectively

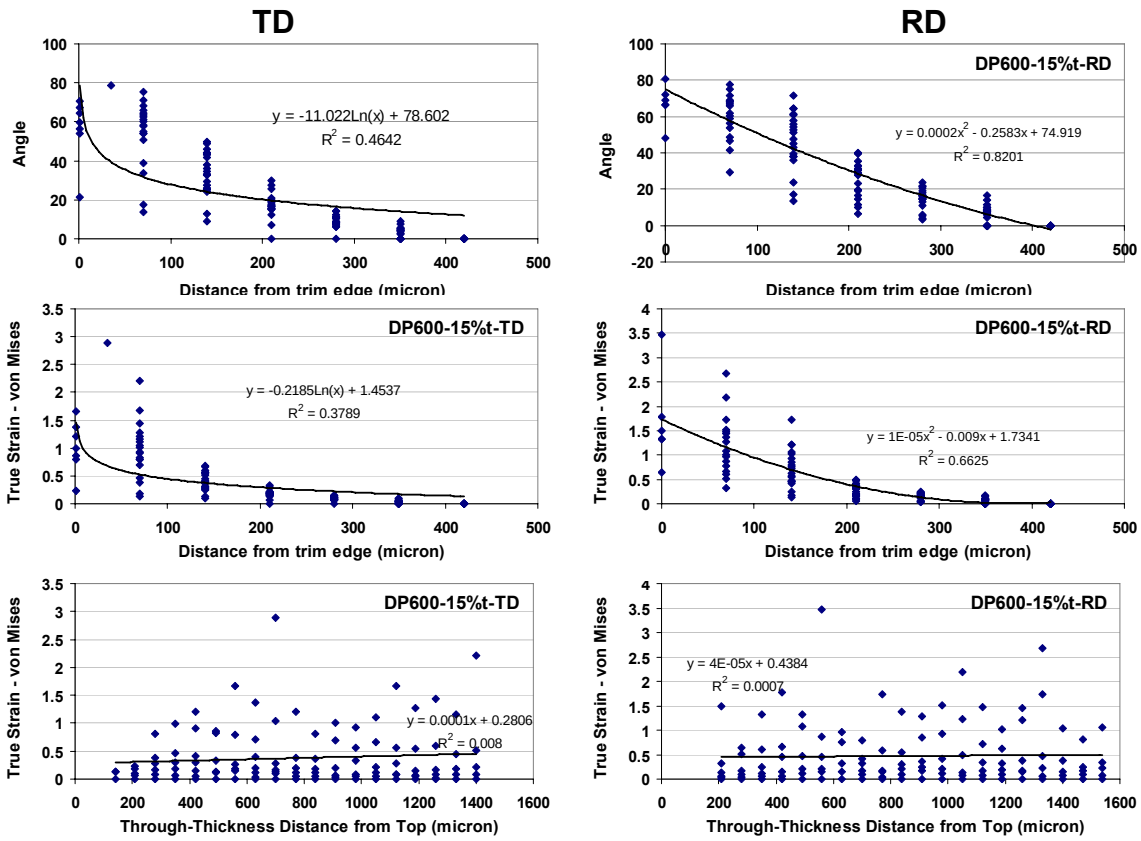

Fig. 17. DP600, 15%t. Similar plots as that in Fig 16.

In order to show the magnitudes and trend of distribution more clearly, one set of the results for DP600 are shown in 1D plot. Fig 16 shows the measured angle distribution in x1 (top),for die clearance of 10%t and Fig 17 for die clearance of 15%t. Other results for DP780 and DP980 are not shown but have similar distribution pattern. The data scattering is mainly from the 2D distribution feature in this 1D plot. The major findings are follows:

(a) From edge to interior (Figs 16 and 17 middle plots):

- The shear strain is high at the edge and monotonically decreases towards interior.
- A very high peak strain (above equivalent true strain of 2) was observed at the fractured edge, for all three DP steels tested. The peak value in the neighborhood of fractured edge reflects the material's fracture strain upon failure under a simple shear loading condition, which is higher than that from usual uniaxial tensile tests.

- The strain decreases rapidly away from the edge: at 300μm the residual is already very low (about 0.2), and at 500μm it diminishes. This defines the shear edge affected zone of 500μm from the edge, which is 31% of the thickness, for a die clearance up to 15%t in this study, which is a regular die clearance range.

(b) From top to bottom of the thickness (Figs 16 and 17 bottom plots):

- There is no clear trend of through-thickness strain change, as the average strain is almost flat over the thickness. This does not include the roll-over zone and top layer, where the tilting angles were not measured, but can be expected to be at relatively lower strain.
- At the very edge (the high bound of the scattered data), the strain shows two peaks. The highest peak appeared within about 1/3~1/2 of the thickness from the top, that approximately corresponds to the burnish zone ending point and below, or at the stage when many microcracks/damages developed to a main crack and ran through the thickness. The second peak appeared at some distance near the bottom when the punch passed about 2/3 of the thickness, probably related to the bottom die support that might postpone the fracture and generated higher strain before final fracture.

5. DISCUSSION

5.1. Completion of crack development from top and bottom cutting edges:

It is notable that the above described shear process in Section 3.3 should apply to both top and bottom parts of the sheet, and the punch and die have equivalent role in the cutting. Therefore, under an idealized condition with a symmetrical deformation zones in top and bottom, the edge profile would be the result of two cracks developed from both top/bottom sides and merge at the mid-plane, if the punch and die have exact the same edge profile and can maintain the same under loading (elastic deformation), and the cutting line (from top view) is straight (plane strain cutting), as shown schematically in Fig 6(f). In reality a perfect symmetry of top/bottom and left/right does not exist, and even it is possible the material properties may not uniform locally and between top and bottom; thus, the crack would have little chance to develop very evenly from both sides and at the same time, despite that the roll-over zone and burnish zone may be

developed similarly from top and bottom in the earlier stage of the shear. The crack initiation and propagation from one side only will dominate the facture zone morphology, and the actual crack path may override the edge feature of burnish zone in other side. Unfortunately in this set of shear experiments performed at an industry site only one side of samples with pierced holes was collected but the other side of removed slugs were not collected, and this edge symmetry issue will need to be further discussed in a separate paper.

For a curved shear edge line (such as the present piercing) the force balance in radial direction requires the two sheared pairs to have slightly different forces, due to existence of a die clearance. With a simple analysis and assuming the total cutting force is concentrated on the cutting edges of punch and die but not distributed on the contacted plane, for a cutting line at a radius of curvature at R and a clearance at δ, the punch edge unit force per edge length would be slightly higher than that one the die edge, for example by 2~5% for the current punch radii and die clearances. Accordingly, the fracture should be easier to develop from punch edge as compared to that from die edge. But this difference is rather minor if considering a large fluctuation of local microstructure (martensite particle distribution.

5.2. Location of the crack initiation:

The fracture may not initiate at the very corner of the tool, but slightly away from it towards punch side wall, due to the existence of small corner radius in an actual tool, and due to a higher compressive hydrostatic stress underneath the tool contact area as compared with that in the lateral area near the sheared surface, which suppresses the fracture and results in fracture initiation at the side wall of tool contact (the end of burnish zone) and the formation of unwanted burr in other side. In addition, the actual fracture zone edge profile can be a summation of multiple microcracking processes, so that the observed rough surface can be the sequence of many microcracks at various length scales within lattice, between grain and phase particles, and among martensite clusters. Understanding the fracture initiation and propagation process may lead to a better control of burnish ending point/fracture zone starting point to achieve burr-free shearing operation and tool design.

Limitation of the current strain measurement and error estimation

Comparison of strain measurement to the strain hardening measurement by nano-indentation

5.3. Possible impact of the sheared edge to stamping edge cracking

In most conventional stamping process design and simulation the initial state of trimmed blank edges are not considered, which works fine for regular steels and more ductile sheet metals, but for AHSS it is not sufficient. Incorporating the initial pre-strain from edge trimming deformation requires two-stage computer simulation dealing with very different mesh size and principal axes from shearing to edge stretching. In addition, from this study a very high edge pre-strain (and accordingly strain hardening) exists that is probably beyond the existing failure criteria used in common FEA simulation; thus, a new fracture criterion is needed that considers non-proportional strain and stress modes and multiple strain path, with material's orientation dependence of fracture. This involves significant new development of fracture mechanics and material science. In this sense, the current work is just a demonstration of such needs from some experimental observations

6. CONCLUSIONS

Mechanically sheared edges of three advanced high strength dual phase steels, DP600, DP780 and DP980, were characterized by hole piercing with different punch-die clearances of 5%t, 10t%, 15%t, and by OM and SEM observations, for the sheared edge in RD and TS directions. The following findings were observed:

(1) The relative heights of four edge zones are measured as a function of punch-die clearance, material strength grade and the sheet orientation in RD and TD. A general trend is that by increasing die clearance, material strength, and cutting line direction angle to RD (from 0˚ - RD to 90˚ – TD):

- Burr height increases;
- Burnish zone height increase and fracture zone height decreases;
- Roll-over zone height decrease but less obvious.

(2) A new method on shear zone strain field measurement was developed based on simple shear assumption, in which the metal flow line tilting angle can be measured and converted to local shear strain and von Mises equivalent strain.

(3) The strain distribution within the sheared deformation zone has been measured for all the shearing conditions studied. The maximum effective strain has reached true strain of 2 at the fractured edge, and it exponentially decays away from the fractured edge. The shear deformation zone size for a 1.6-mm thick DP steels is about 500 μm from the fractured edge (or about 31% sheet thickness).

(4) This very high edge strain from mechanical shearing will become a severe pre-strain to the proceeding stamping operation and potentially give significant impact to edge cracking in stamping of DP steels involving edge stretching, which needs to be considered for stamping simulation.

From the above observations new understandings were obtained on shear fracture process and related mechanics, important to further develop tool design strategy for a given material that can reduce burr formation and edge defects:

(1) Inhomogeneous microstructures and the existence of two phases (martensite and ferrite) with significantly different properties play very important role in edge shear fracture process. Depending on the martensite distribution feature, multiple cracks may develop along the martensite cluster boundaries, initiate at different locations and time, and develop at different stages. The final failure is the result of multiple crack development, with a major crack links multiple microcracks and passes through the thickness, forming complex morphology of surface fracture;

(2) Upon failure many sub-cracks with incomplete development form "Λ"-shaped surface cracks or sink patches in both burnish zone and fractured zone, depending on the sub-crack surrounded volume.

(3) The formation of four characteristic edge feature zones is the results of group events of multiple crack initiation-propagation processes, which, for high strength dual phase steels, has a random nature. As a result, four edge zones may not completely form at a relatively high probability as compared to regular steels.

Appendix

In sheet metal cutting the cutting line dimension is much larger than the sheet thickness, so the plane strain deformation condition applies and no displacement and strain in y direction (along the cutting line). Further more, with a small punch-die clearance gap and with a firm clamping of the sheet, the displacements in x_1 direction (the radial direction here) is largely constrained, and the displacement in x_3 direction is allowed, but the total thickness of the sheet within the sheared zone remains almost unchanged (if the micro-cavitation is not considered and the volume conservation applies for plastic deformation). Thus, the displacement components u=0 and v=0 in x, y directions but $w \neq 0$ in z direction, and the strain components are all equal or close to zero except for $\varepsilon_{xz} \neq 0$. This is very close to a simple shear deformation condition.

$$\bar{\varepsilon} = \sqrt{\frac{2}{3}\left(\varepsilon_1^{\,2} + \varepsilon_2^{\,2}\right)} = \frac{2}{\sqrt{3}}\varepsilon_{12} = \frac{1}{\sqrt{3}}\gamma_{12} = \frac{1}{\sqrt{3}}\tan(\alpha) \quad (3)$$

On Simple shear test

Small deformation formulation: With small strain tensor component formulation [19]

$$\varepsilon_{ij} = \frac{1}{2}\left(\frac{\partial u_j}{\partial x_i} + \frac{\partial u_i}{\partial x_j}\right), \textit{(i, j = x, z and } \kappa \textit{ is a dummy index)} \quad (1)$$

With simple shear assumption and with u=0, $\frac{\partial w}{\partial x} = k = \tan(\alpha)$, where k is the slope of the flow line in deformed sample coordinate. This gives only one non-zero component, i.e.

$$\varepsilon_{xz} = \frac{1}{2}\left\{\frac{\partial w}{\partial x}\right\} = 0.5\,k = 0.5\,\tan(\alpha) = 0.5\,\gamma_{xz} \quad (2)$$

Here γ_{xz} is engineering shear strain (and also the slope of the measured flow line tilting angle). Accordingly von Mises effective strain is

$$\varepsilon_{eff} = \sqrt{\frac{2}{9}\left[(\varepsilon_1 - \varepsilon_1)^2 + (\varepsilon_1 - \varepsilon_1)^2 + (\varepsilon_1 - \varepsilon_1)^2 + 6(\varepsilon_{12}{}^2 + \varepsilon_{23}{}^2 + \varepsilon_{13}{}^2)\right]} = \frac{2}{\sqrt{3}}\varepsilon_{13} = \frac{1}{\sqrt{3}}k \qquad (3)$$

Finite deformation formulation: based on classical tensor analysis, the finite strain sensor components in (x, z) plane can be generally expressed as (see Appendix for more detail)

$$\varepsilon_{ij} = \frac{1}{2}\left(\frac{\partial u_j}{\partial x_i} + \frac{\partial u_i}{\partial x_j} + \frac{\partial u_k}{\partial x_i}\frac{\partial u_k}{\partial x_j}\right), \textit{(i, j = x, z and } \kappa \textit{ is a dummy index)} \qquad (4)$$

Here the second-order derivatives need to be considered. By expansion the true strain tensor components in the shear plane (x,z) are

$$\varepsilon_{xx} = \frac{1}{2}\left(\frac{\partial w}{\partial x}\right)^2 = 0.5\ \kappa^2 \qquad (5)$$

$$\varepsilon_{xz} = \frac{1}{2}\left\{\frac{\partial w}{\partial x}\right\} = 0.5\ \kappa \qquad (6)$$

All other components are zero, and von Mises effective strain is given by

$$\varepsilon_{eff} = \sqrt{\frac{2}{9}\left[(\varepsilon_{xx} - \varepsilon_{yy})^2 + (\varepsilon_{yy} - \varepsilon_{zz})^2 + (\varepsilon_{zz} - \varepsilon_{xx})^2 + 6(\varepsilon_{xy}{}^2 + \varepsilon_{yz}{}^2 + \varepsilon_{zx}{}^2)\right]}$$

$$= \frac{2}{3}\sqrt{\varepsilon_{xx}{}^2 + 3\varepsilon_{xz}{}^2} \qquad (7)$$

Or,

$$\boxed{\varepsilon_{eff} = \frac{k}{3}\sqrt{3 + k^2}} \qquad (8)$$

At small k we may ignore the term k^2, and Eq (8) reduces to Eq (3).

For small strain the strain tensor components can be formulated as

$$\varepsilon_{ij} = \frac{1}{2}\left(\frac{\partial u_i}{\partial x_j} + \frac{\partial u_j}{\partial x_i}\right),$$

And in the simple shear in 1-3 plane the measured shear angle is related to the shear strain (without considering the rigid rotation of the element) by

$\gamma_{13} = 2\varepsilon_{13}$

The derivation of Eq () can be found in Ref [19]. For the 2D analysis of small strain $i \neq j$

Based on classical tensor analysis, the finite strain sensor components are given in the deformed specimen coordinates (x-z) plane as

$$\varepsilon_{ij} = \frac{1}{2}\left(\frac{\partial u_j}{\partial x_i} + \frac{\partial u_i}{\partial x_j} + \frac{\partial u_k}{\partial x_i}\frac{\partial u_k}{\partial x_j} \right), \textit{(i, j = x, z and } \kappa \textit{ is a dummy index)} \quad (1)$$

Or, for with expansion,

$$E_{xx} = \frac{\partial u}{\partial x} + \frac{1}{2}\left\{ \left(\frac{\partial u}{\partial x} \right)^2 + \left(\frac{\partial w}{\partial x} \right)^2 \right\}$$

$$E_{zz} = \frac{\partial w}{\partial z} + \frac{1}{2}\left\{ \left(\frac{\partial u}{\partial z} \right)^2 + \left(\frac{\partial w}{\partial z} \right)^2 \right\}$$

$$E_{xy} = \frac{1}{2}\left\{ \frac{\partial w}{\partial x} + \frac{\partial u}{\partial z} + \frac{\partial u}{\partial x}\frac{\partial u}{\partial z} + \frac{\partial w}{\partial x}\frac{\partial w}{\partial z} \right\}$$

In the current experimental condition with a full constraint in x direction, u=0, $\frac{\partial w}{\partial x} = \alpha$, and $\frac{\partial w}{\partial z} \approx 0$; thus, the true strain tensor components in the shear plane (x,y) are

$$\varepsilon_{xx} = \frac{1}{2}\left(\frac{\partial w}{\partial x} \right)^2 = 0.5\,\alpha^2$$

$$\varepsilon_{yy} = 0$$

$$\varepsilon_{xy} = \frac{1}{2}\left\{ \frac{\partial v}{\partial x} \right\} = 0.5\,\alpha$$

With all components in z direction to be zero, and the von Mises effective strain is given by

$$\varepsilon_{eff} = \sqrt{\frac{2}{9}\left[\left(\varepsilon_{xx} - \varepsilon_{yy}\right)^2 + \left(\varepsilon_{yy} - \varepsilon_{zz}\right)^2 + \left(\varepsilon_{zz} - \varepsilon_{xx}\right)^2 + 6\left(\varepsilon_{xy}{}^2 + \varepsilon_{yz}{}^2 + \varepsilon_{zx}{}^2\right) \right]}$$

$$= \frac{2}{3}\sqrt{\varepsilon_{xx}{}^2 + 3\varepsilon_{xy}{}^2}$$

$$\boxed{\varepsilon_{eff} = \frac{1}{3}\sqrt{3\alpha^2 + \alpha^4}}$$

Appendix:

Point transformation:

The coordinate of a point P can be expressed either in Eulerian coordinate xi, or in sample coordinate X (Lagrangian coordinate). The conversion between x and X can be expressed as:

$$X=f(x), \tag{1}$$

and the inverse function

$$x=g(X), \tag{2}$$

for every point of the body. The conversions are assumed to be continuous and differentiable.

Consider an infinitesimal line element connecting the point P(x) to its neighboring point P′(x+dx), the initial length of PP′ can be expressed in the coordinate system x as

$$ds_0 = dx = \frac{\partial g}{\partial X_i} dX_i = a_{ij} \frac{\partial X_i}{\partial x_m} \frac{\partial X_j}{\partial x_n} dx^m dx^n \tag{3}$$

When P-P′ is deformed to the points Q(X) and Q′(X+dX), the deformed length QQ′ can be expressed in the coordinate system X as

$$ds = dX = \frac{\partial f}{\partial x_i} dx_i = b_{ij} \frac{\partial x_i}{\partial X_m} \frac{\partial x_j}{\partial X_n} dX^m dX^n \tag{4}$$

where a_{ij} and b_{ij} are the Euclidean metric tensor for the coordinate system x and X, evaluated at the point P.

The square of the length is

$$ds^2 - ds_o^2 = \left(a_{\alpha\beta} \frac{\partial X_\alpha}{\partial x_i} \frac{\partial X_\beta}{\partial x_j} - b_{ij} \right) dx^i dx^j = 2E_{ij} dx^i dx^j$$

$$ds^2 - ds_o^2 = \left(a_{ij} - b_{\alpha\beta} \frac{\partial x_\alpha}{\partial X_i} \frac{\partial x_\beta}{\partial X_j} \right) dX^i dX^j = 2e_{ij} dX^i dX^j \tag{5}$$

here

$$E_{ij} = \frac{1}{2} \left(a_{\alpha\beta} \frac{\partial X_\alpha}{\partial x_i} \frac{\partial X_\beta}{\partial x_j} - b_{ij} \right)$$

is called Green's strain tensor, introduced by Green and St. Venant. It is often referred to as a strain tensor in Lagrangian coordinates.

$$e_{ij} = \frac{1}{2} \left(a_{ij} - b_{\alpha\beta} \frac{\partial x_\alpha}{\partial X_i} \frac{\partial x_\beta}{\partial X_j} \right)$$

The strain tensor eij was introduced by Cauchy for infinitesimal strain.

If we use rectangular Cartesian coordinates (rectilinear and orthogonal) to describe both the original and the deformed configurations of a body, then

$$a_{ij} = b_{ij} = \delta_{ij} = \begin{matrix} 1(i = j) \\ 0(i \neq j) \end{matrix}.$$

we use the displacement vector u

$X_i = x_i + u_i$, or $x_i = X_i - u_i$. Then we have

$$\frac{\partial X_\alpha}{\partial x_i} = \frac{\partial u_\alpha}{\partial x_i} + \delta_{\alpha j} \text{ and } \frac{\partial x_\alpha}{\partial X_i} = \delta_{\alpha j} - \frac{\partial u_\alpha}{\partial X_i}$$

The strain tensors reduce to the simple form,

$$E_{ij} = \frac{1}{2}\left(\delta_{\alpha\beta} \frac{\partial X_\alpha}{\partial x_i} \frac{\partial X_\beta}{\partial x_j} - \delta_{ij} \right)$$

$$= \frac{1}{2}\left[\delta_{\alpha\beta} \left(\frac{\partial u_\alpha}{\partial x_i} + \delta_{\alpha j} \right) \left(\frac{\partial u_\beta}{\partial x_j} + \delta_{\beta j} \right) - \delta_{ij} \right]$$

$$= \frac{1}{2}\left[\frac{\partial u_j}{\partial x_i} + \frac{\partial u_i}{\partial x_j} + \frac{\partial u_\alpha}{\partial x_i} \frac{\partial u_\beta}{\partial x_j} \right]$$

Or in the expanded form,

$$E_{xx} = \frac{\partial u}{\partial x} + \frac{1}{2}\left\{ \left(\frac{\partial u}{\partial x} \right)^2 + \left(\frac{\partial v}{\partial x} \right)^2 + \left(\frac{\partial w}{\partial x} \right)^2 \right\}$$

$$E_{yy} = \frac{\partial u}{\partial y} + \frac{1}{2}\left\{ \left(\frac{\partial u}{\partial y} \right)^2 + \left(\frac{\partial v}{\partial y} \right)^2 + \left(\frac{\partial w}{\partial y} \right)^2 \right\}$$

$$E_{xy} = \frac{1}{2}\left\{ \frac{\partial u}{\partial y} + \frac{\partial v}{\partial x} + \frac{\partial u}{\partial x}\frac{\partial u}{\partial y} + \frac{\partial v}{\partial x}\frac{\partial v}{\partial y} + \frac{\partial w}{\partial x}\frac{\partial w}{\partial y} \right\}$$

and so on for other two planes.

======

Similarly,

$$e_{ij} = \frac{1}{2}\left[\frac{\partial u_j}{\partial X_i} + \frac{\partial u_i}{\partial X_j} - \frac{\partial u_\alpha}{\partial X_i} \frac{\partial u_\beta}{\partial X_j} \right]$$

is called Green's strain tensor, introduced by Green and St. Venant.

$$e_{ij}=\frac{1}{2}\left(a_{ij} - b_{\alpha\beta}\frac{\partial x_\alpha}{\partial X_i}\frac{\partial x_\beta}{\partial X_j}\right)$$

Ui = Xi-xi

ds of the element QQ′ is dX, or

$$ds^2 - ds_o^2 = a_{ij}dx^i dx^j, \quad (3)$$

$$ds^2=g_{ij}dX^i dX^j \quad (4)$$

where g_{ij} is the Euclidean metrix tensor for the coordinate system X.

Thus, from Eqs (3,4)

Ds-dso =

Assume a continuous and one-to-one point transformation (mapping) of coordinate from point P to point Q, the change of configuration of the body

References

[1] W. Johnson, S. K. Ghosh, and S. R. Reid, "PIERCING AND HOLE-FLANGING OF SHEET METALS - A SURVEY," *Memoires Scientifiques De La Revue De Metallurgie,* vol. 77, pp. 585-606, 1980.

[2] R. Hambli and F. Guerin, "Application of a neural network for optimum clearance prediction in sheet metal blanking processes," *Finite Elements in Analysis and Design,* vol. 39, pp. 1039-1052, 2003.

[3] K. Hasegawa, K. Kawamura, T. Urabe, and Y. Hosoya, "Effects of microstructure on stretch-flange-formability of 980 MPa grade cold-rolled ultra high strength steel sheets," *Isij International,* vol. 44, pp. 603-609, 2004.

[4] K. H. Shim, S. K. Lee, B. S. Kang, and S. M. Hwang, "Investigation on blanking of thin sheet metal using the ductile fracture criterion and its experimental verification," *Journal of Materials Processing Technology,* vol. 155-156, pp. 1935-1942, 2004.

[5] J. Mediavilla, R. H. J. Peerlings, and M. G. D. Geers, "An integrated continuous-discontinuous approach towards damage engineering in sheet metal forming processes," *Engineering Fracture Mechanics,* vol. 73, pp. 895-916, 2006.

[6] F. Gréban, G. Monteil, and X. Roizard, "Influence of the structure of blanked materials upon the blanking quality of copper alloys," *Journal of Materials Processing Technology,* vol. 186, pp. 27-32, 2007.

[7] S.-P. Lo, D.-Y. Chang, and Y.-Y. Lin, "Quality prediction model of the sheet blanking process for thin phosphorous bronze," *Journal of Materials Processing Technology,* vol. 194, pp. 126-133, 2007.

[8] S. Thipprakmas, M. Jin, and M. Murakawa, "Study on flanged shapes in fineblanked-hole flanging process (FB-hole flanging process) using finite element method (FEM)," *Journal of Materials Processing Technology,* vol. 192-193, pp. 128-133, 2007.

[9] S. Thipprakmas, M. Jin, and M. Murakawa, "An investigation of material flow analysis in fineblanking process," *Journal of Materials Processing Technology,* vol. 192-193, pp. 237-242, 2007.
[10] G. J. A. Bing and J. Wallbank, "The effect of using a sprung stripper in sheet metal cutting," *Journal of Materials Processing Technology,* vol. 200, pp. 176-184, 2008.
[11] C. Husson, J. P. M. Correia, L. Daridon, and S. Ahzi, "Finite elements simulations of thin copper sheets blanking: Study of blanking parameters on sheared edge quality," *Journal of Materials Processing Technology,* vol. 199, pp. 74-83, 2008.
[12] V. Lemiale, J. Chambert, and P. Picart, "Description of numerical techniques with the aim of predicting the sheet metal blanking process by FEM simulation," *Journal of Materials Processing Technology,* vol. In Press, Corrected Proof, 2008.
[13] H. Marouani, A. Ben Ismail, E. Hug, and M. Rachik, "Rate-dependent constitutive model for sheet metal blanking investigation," *Materials Science and Engineering a-Structural Materials Properties Microstructure and Processing,* vol. 487, pp. 162-170, Jul 2008.
[14] S. Thipprakmas, S. Rojananan, and P. Paramaputi, "An investigation of step taper-shaped punch in piercing process using finite element method," *Journal of Materials Processing Technology,* vol. 197, pp. 132-139, 2008.
[15] G. Buzzichelli and E. Anelli, "Present status and perspectives of European research in the field of advanced structural steels," *Isij International,* vol. 42, pp. 1354-1363, 2002.
[16] S. Auto/Steel Partnership, Michigan, "Advanced High-Strength Steel Product and Process Applications Guidelines: A Special Edition of In-Depth AHSS Case Studies," April 2008.
[17] I. I. S. I. C. o. A. Applications, "Advanced High-Strength Steels Application Guidelines Version 3," *http://www.worldautosteel.org/newsrelease.do?id=70#*, September 2006.
[18] Z. Marciniak, J. L. Duncan, and s. J. Hu, *Mechanics of Sheet Metal Forming*, 2nd ed. Ann Arbor: Butterworth-Heinemann, 2002.
[19] W. F. Hosford and R. M. Caddell, *Metal Forming (2nd edition)*. New Jersey 07632: Prentice-Hall, Inc., 1993.